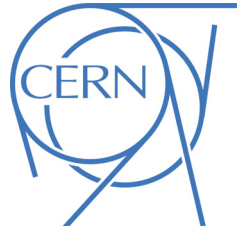




ATLAS NOTE

ATLAS-CONF-2013-047

May 16, 2013
Revision: June 30, 2013



Search for squarks and gluinos with the ATLAS detector in final states with jets and missing transverse momentum and 20.3 fb^{-1} of $\sqrt{s} = 8 \text{ TeV}$ proton-proton collision data

ATLAS Collaboration

Abstract

A search for squarks and gluinos in final states containing high- p_T jets, missing transverse momentum and no electrons or muons is presented. The data were recorded in 2012 by the ATLAS experiment in $\sqrt{s} = 8 \text{ TeV}$ proton-proton collisions at the Large Hadron Collider, with a total integrated luminosity of 20.3 fb^{-1} . No significant excess above the Standard Model expectation is observed. In a simplified model with only gluinos and the lightest neutralino, gluino masses below 1350 GeV are excluded at the 95% confidence level when the lightest neutralino is massless. For a simplified model involving the strong production of squarks of the first two generations, with decays to a massless lightest neutralino, squark masses below 780 GeV are excluded. In MSUGRA/CMSSM models with $\tan\beta = 30$, $A_0 = -2m_0$ and $\mu > 0$, squarks and gluinos of equal mass are excluded for masses below 1700 GeV. These limits extend the region of supersymmetric parameter space excluded by previous searches with the ATLAS detector.

The following have been revised with respect to the version dated May 16, 2013: squark mass contours in Figures 5 and 16 (left), $m_{\tilde{g}} - m_{\tilde{q}}$ plane exclusion limits in Figures 5 and 16 (right) and mass limit values for the MSUGRA/CMSSM scenario; cross-sections and resulting exclusion limits for the simplified phenomenological MSSM scenario (Figures 6 and 17).

1 Introduction

Many extensions of the Standard Model (SM) include heavy coloured particles, some of which could be accessible at the Large Hadron Collider (LHC) [1]. The squarks and gluinos of supersymmetric (SUSY) theories [2–10] form one class of such particles. This note presents a new ATLAS search for squarks and gluinos in final states containing only jets and large missing transverse momentum. Interest in this final state is motivated by the large number of R -parity conserving models [11–15] in which squarks, \tilde{q} , and gluinos, \tilde{g} , can be produced in pairs $\{\tilde{g}\tilde{g}, \tilde{q}\tilde{q}, \tilde{q}\tilde{g}\}$ and can decay through $\tilde{q} \rightarrow q\tilde{\chi}_1^0$ and $\tilde{g} \rightarrow q\bar{q}\tilde{\chi}_1^0$ to weakly interacting lightest neutralinos, $\tilde{\chi}_1^0$. The $\tilde{\chi}_1^0$ is the lightest SUSY particle (LSP) and escapes the detector unseen. The analysis presented here updates previous ATLAS results obtained using similar selections [16–19]. Events with reconstructed electrons or muons are vetoed to avoid overlap with a related ATLAS search [20, 21]. The search strategy was optimised in the $(m_{\tilde{g}}, m_{\tilde{q}})$ -plane (where $m_{\tilde{g}}, m_{\tilde{q}}$ are the gluino and squark masses respectively) for a range of models, including a simplified one in which all other supersymmetric particles, except for the lightest neutralino, were given masses beyond the reach of the LHC. Although mostly interpreted in terms of SUSY models, the main results of this analysis (the data and expected background event counts in the signal regions) are relevant for constraining any model of new physics that predicts production of jets in association with missing transverse momentum.

2 The ATLAS Detector and Data Samples

The ATLAS detector [22] is a multipurpose particle physics detector with a forward-backward symmetric cylindrical geometry and nearly 4π coverage in solid angle.¹ The layout of the detector features four superconducting magnet systems, which comprise a thin solenoid surrounding inner tracking detectors (covering $|\eta| < 2.5$) and three large toroids supporting a muon spectrometer (covering $|\eta| < 2.5$). The calorimeters are of particular importance to this analysis. In the pseudorapidity region $|\eta| < 3.2$, high-granularity liquid-argon (LAr) electromagnetic (EM) sampling calorimeters are used. An iron/scintillator-tile calorimeter provides hadronic coverage over $|\eta| < 1.7$. The end-cap and forward regions, spanning $1.5 < |\eta| < 4.9$, are instrumented with LAr calorimeters for both EM and hadronic measurements.

The data sample used in this analysis was collected in 2012 with the LHC operating at a centre-of-mass energy of 8 TeV. Application of beam, detector and data-quality requirements resulted in a total integrated luminosity of 20.3 fb^{-1} . The uncertainty on the integrated luminosity is $\pm 2.8\%$, derived by following the same methodology as that detailed in Ref. [23] using a preliminary calibration of the luminosity scale derived from beam-separation scans performed in November 2012. The trigger required events to contain a leading jet with an uncorrected transverse momentum (p_T) above 80 GeV and an uncorrected missing transverse momentum above 100 GeV. The trigger reached its full efficiency for events with a reconstructed jet with p_T exceeding 130 GeV and more than 160 GeV of missing transverse momentum. For the data sample studied the trigger is fully efficient.

3 Object Reconstruction

Jet candidates are reconstructed using the anti- k_t jet clustering algorithm [24, 25] with a radius parameter of 0.4. The inputs to this algorithm are clusters [26, 27] of calorimeter cells seeded by those with energy significantly above the measured noise. Jet momenta are constructed by performing a four-vector sum

¹ ATLAS uses a right-handed coordinate system with its origin at the nominal interaction point in the centre of the detector and the z -axis along the beam pipe. Cylindrical coordinates (r, ϕ) are used in the transverse plane, ϕ being the azimuthal angle around the beam pipe. The pseudorapidity η is defined in terms of the polar angle θ by $\eta = -\ln \tan(\theta/2)$.

over these cell clusters, treating each as an (E, \vec{p}) four-vector with zero mass. The jets are corrected for energy from additional proton-proton collisions in the same or neighbouring bunch crossings (pile-up) using a method, suggested in Ref. [28], which estimates the pile-up activity in any given event, as well as the sensitivity of any given jet to pile-up. The method subtracts a contribution from the jet energy equal to the product of the jet area and the event average energy density. The local cluster weighting (LCW) jet calibration method [26, 29] is used to classify topological cell clusters within the jets as either being of electromagnetic or hadronic origin and based on this classification applies specific energy corrections derived from a combination of Monte Carlo (MC) simulation and data. Further corrections, referred to as ‘jet energy scale’ or ‘JES’ corrections below, are derived from MC and data and used to calibrate the energies of jets to the mean scale of their constituent particles [26]. Only jet candidates with $p_T > 20$ GeV after all corrections are retained. Jets are identified as originating from heavy-flavour decays using the ‘MV1’ neural network based b -tagging algorithm with a 70% efficiency operating point [30]. Candidate b -tagged jets must possess $p_T > 40$ GeV and $|\eta| < 2.5$.

Electron candidates are required to have $p_T > 10$ GeV and $|\eta| < 2.47$, and to pass electron shower shape and track selection criteria based upon those described in Ref. [31], but modified to reduce the impact of pile-up and to match tightened trigger requirements. Muon candidates are formed by combining information from the muon spectrometer and inner tracking detectors as described in Refs. [32, 33] and are required to have $p_T > 10$ GeV and $|\eta| < 2.4$. Reconstructed photons are used to constrain $Z + \text{jet}$ backgrounds (see below), although they are not used in the main analysis. Photon candidates are required to possess $p_T > 130$ GeV and $|\eta| < 1.37$ or $1.52 < |\eta| < 2.47$, and to pass photon shower shape and electron rejection criteria [34].

Following the steps above, overlaps between candidate jets with $|\eta| < 2.8$ and leptons (electrons or muons) are resolved as follows. First, any such jet candidate lying within a distance $\Delta R \equiv \sqrt{(\Delta\eta)^2 + (\Delta\phi)^2} = 0.2$ of an electron is discarded; then any lepton candidate remaining within a distance $\Delta R = 0.4$ of any surviving jet candidate is discarded.

The measurement of the missing transverse momentum two-dimensional vector $\mathbf{E}_T^{\text{miss}}$ (and its magnitude E_T^{miss}) is based on the calibrated transverse momenta of all jet and lepton candidates and all calorimeter clusters not associated to such objects [35]. Following this step, all jet candidates with $|\eta| > 2.8$ are discarded. Thereafter, the remaining lepton and jet candidates are considered “reconstructed”, and the term “candidate” is dropped.

4 Signal and Control Region Definitions

Following the object reconstruction described above, events are discarded if any electrons or muons with $p_T > 10$ GeV remain, or if they have any jets failing quality selection criteria designed to suppress detector noise and non-collision backgrounds (see e.g. Ref. [36]), or if they lack a reconstructed primary vertex associated with five or more tracks. The criteria applied to jets include requirements on the fraction of the transverse momentum of the jet carried by charged tracks, and on the fraction of the jet energy contained in the electromagnetic layers of the calorimeter. A consequence of these requirements is that events containing hard photons have a high probability of failing the signal region selection criteria.

This analysis aims to search for the production of heavy SUSY particles decaying into jets and stable lightest neutralinos, with the latter creating missing transverse momentum. Because of the high mass scale expected for the SUSY signal, the ‘effective mass’, m_{eff} , is a powerful discriminant between the signal and most Standard Model backgrounds. When selecting events with at least N jets, m_{eff} is defined to be the scalar sum of the transverse momenta of the leading N jets and E_T^{miss} . The final signal selection uses requirements on $m_{\text{eff}}(\text{incl.})$, which sums over all jets with $p_T > 40$ GeV and E_T^{miss} . Requirements placed on m_{eff} and E_T^{miss} , which suppress the multi-jet background, formed the basis of the previous ATLAS jets + E_T^{miss} + 0-lepton SUSY searches [17–19]. The same strategy is adopted in this analysis.

Requirement	Channel									
	A (2-jets)		B (3-jets)		C (4-jets)		D (5-jets)	E (6-jets)		
	L	M	M	T	M	T	—	L	M	T
$E_T^{\text{miss}} [\text{GeV}] >$	160									
$p_T(j_1) [\text{GeV}] >$	130									
$p_T(j_2) [\text{GeV}] >$	60									
$p_T(j_3) [\text{GeV}] >$	—	60		60		60	60			
$p_T(j_4) [\text{GeV}] >$	—	—		60		60	60			
$p_T(j_5) [\text{GeV}] >$	—	—		—		60	60			
$p_T(j_6) [\text{GeV}] >$	—	—		—		—	60			
$\Delta\phi(\text{jet}_i, \mathbf{E}_T^{\text{miss}})_{\text{min}} >$	$0.4 (i = \{1, 2, (3 \text{ if } p_T(j_3) > 40 \text{ GeV})\})$				$0.4 (i = \{1, 2, 3\}), 0.2 (p_T > 40 \text{ GeV jets})$					
$E_T^{\text{miss}} / m_{\text{eff}}(Nj) >$	0.2	— ^a	0.3	0.4	0.25	0.25	0.2	0.15	0.2	0.25
$m_{\text{eff}}(\text{incl.}) [\text{GeV}] >$	1000	1600	1800	2200	1200	2200	1600	1000	1200	1500

(a) For SR A-medium the cut on $E_T^{\text{miss}} / m_{\text{eff}}(Nj)$ is replaced by a requirement $E_T^{\text{miss}} / \sqrt{H_T} > 15 \text{ GeV}^{1/2}$.

Table 1: Selection criteria used to define each of the channels in the analysis. Each channel is divided into between one and three signal regions on the basis of the requirements listed in the bottom two rows. The signal regions are indicated in the third row from the top and are denoted ‘loose’ (L), ‘medium’ (M) and ‘tight’ (T). The $E_T^{\text{miss}} / m_{\text{eff}}$ cut in any N jet channel uses a value of m_{eff} constructed from only the leading N jets (indicated in parentheses in the second row). However, the final $m_{\text{eff}}(\text{incl.})$ selection, which is used to define the signal regions, includes all jets with $p_T > 40 \text{ GeV}$.

The requirements used to select jets and leptons are chosen to give sensitivity to a broad range of SUSY models. In order to achieve maximal reach over the $(m_{\tilde{q}}, m_{\tilde{q}})$ -plane, several analysis channels are defined. Squarks typically generate at least one jet in their decays, for instance through $\tilde{q} \rightarrow q\tilde{\chi}_1^0$, while gluinos typically generate at least two jets, for instance through $\tilde{g} \rightarrow q\bar{q}\tilde{\chi}_1^0$. Processes contributing to $\tilde{q}\tilde{q}$, $\tilde{q}\tilde{g}$ and $\tilde{g}\tilde{g}$ final states therefore lead to events containing at least two, three or four jets, respectively. Decays of heavy SUSY and SM particles produced in \tilde{q} and \tilde{g} cascades tend to further increase the final state multiplicity.

Five inclusive analysis channels, labelled A to E and characterised by increasing jet multiplicity from two to six, are defined in Table 1. Each channel is used to construct between one and three signal regions (SRs) with ‘loose’, ‘medium’, or ‘tight’ selections distinguished by requirements placed on $E_T^{\text{miss}} / m_{\text{eff}}$ and $m_{\text{eff}}(\text{incl.})$. The lower jet multiplicity channels focus on models characterised by squark pair production with short decay chains, while those requiring high jet multiplicity are optimised for gluino pair production and/or long cascade decay chains. In SR A-medium the cut on $E_T^{\text{miss}} / m_{\text{eff}}$ is replaced by a requirement on $E_T^{\text{miss}} / \sqrt{H_T}$ (where H_T is defined as the scalar sum of the transverse momenta of all $p_T > 40 \text{ GeV}$ jets), which has been found to lead to enhanced sensitivity to models characterised by $\tilde{q}\tilde{q}$ production with a large $\tilde{q}-\tilde{\chi}_1^0$ mass splitting.

In Table 1, $\Delta\phi(\text{jet}, \mathbf{E}_T^{\text{miss}})_{\text{min}}$ is the smallest of the azimuthal separations between $\mathbf{E}_T^{\text{miss}}$ and the reconstructed jets. For channels A and B, the selection requires $\Delta\phi(\text{jet}, \mathbf{E}_T^{\text{miss}})_{\text{min}} > 0.4$ using up to three leading jets with $p_T > 40 \text{ GeV}$ if present in the event. For the other channels an additional requirement $\Delta\phi(\text{jet}, \mathbf{E}_T^{\text{miss}})_{\text{min}} > 0.2$ is placed on all jets with $p_T > 40 \text{ GeV}$. Requirements on $\Delta\phi(\text{jet}, \mathbf{E}_T^{\text{miss}})_{\text{min}}$ and $E_T^{\text{miss}} / m_{\text{eff}}$ are designed to reduce the background from multi-jet processes.

Standard Model background processes contribute to the event counts in the signal regions. The dominant sources are: $W+\text{jets}$, $Z+\text{jets}$, top quark pairs, single top quarks, and multiple jets. The production of semi-leptonically decaying dibosons is a small component (<13%) of the total background and

CR	SR background	CR process	CR selection
CRY	$Z(\rightarrow \nu\nu) + \text{jets}$	$\gamma + \text{jets}$	Isolated photon
CRQ	multi-jets	multi-jets	Reversed $\Delta\phi(\text{jet}, \mathbf{E}_T^{\text{miss}})_{\text{min}}$ and $E_T^{\text{miss}}/m_{\text{eff}}(Nj)$ requirements ^a
CRW	$W(\rightarrow \ell\nu) + \text{jets}$	$W(\rightarrow \ell\nu) + \text{jets}$	$30 \text{ GeV} < m_T(\ell, \mathbf{E}_T^{\text{miss}}) < 100 \text{ GeV}$, b -veto
CRT	$t\bar{t}$ and single- t	$t\bar{t} \rightarrow bbqq'\ell\nu$	$30 \text{ GeV} < m_T(\ell, \mathbf{E}_T^{\text{miss}}) < 100 \text{ GeV}$, b -tag

(a) For SR A-medium the selection requirement placed on $E_T^{\text{miss}}/\sqrt{H_T}$ is reversed.

Table 2: Control regions used in the analysis: the main targeted background in the SR, the process used to model the background, and main CR cut(s) used to select this process are given. The transverse momenta of leptons(photon) used to select CR events must exceed 25(130) GeV.

is estimated with MC simulated data normalised to theoretical cross-section predictions. The majority of the $W + \text{jets}$ background is composed of $W \rightarrow \tau\nu$ events, with the τ -lepton decaying to hadrons, or $W \rightarrow e\nu, \mu\nu$ events in which no electron or muon candidate is reconstructed. The largest part of the $Z + \text{jets}$ background comes from the irreducible component in which $Z \rightarrow \nu\bar{\nu}$ decays generate large E_T^{miss} . Top quark pair production followed by semi-leptonic decays, in particular $t\bar{t} \rightarrow b\bar{b}\tau\nu qq'$ with the τ -lepton decaying to hadrons, as well as single top quark events, can also generate large E_T^{miss} and pass the jet and lepton requirements at a non-negligible rate. The multi-jet background in the signal regions is caused by misreconstruction of jet energies in the calorimeters leading to apparent missing transverse momentum, as well as by neutrino production in semileptonic decays of heavy quarks. Extensive validation of the Monte Carlo simulation against data has been performed for each of these background sources and for a wide variety of control regions (CRs).

To estimate the backgrounds in a consistent and robust fashion, four control regions are defined for each of the 10 signal regions, giving 40 CRs in total. The orthogonal CR event selections are designed to provide independent data samples enriched in particular background sources. Each ensemble of one SR and four CRs constitutes a different ‘stream’ of the analysis. The CR selections are optimised to maintain adequate statistical weight and low SUSY signal contamination, while minimising as far as possible the systematic uncertainties arising from the extrapolation to the SR.

The CRs are listed in Table 2. CRY is used to estimate the contribution of $Z(\rightarrow \nu\nu) + \text{jets}$ background events to each SR by selecting a sample of $\gamma + \text{jets}$ events with $p_T(\gamma) > 130$ GeV. CRQ uses reversed selection requirements placed on $\Delta\phi(\text{jet}, \mathbf{E}_T^{\text{miss}})_{\text{min}}$ and on $E_T^{\text{miss}}/m_{\text{eff}}(Nj)$ ($E_T^{\text{miss}}/\sqrt{H_T}$ in SR A-medium) to produce data samples enriched in multi-jet background events. CRW and CRT use respectively a b -jet veto or b -jet requirement together with a requirement on the transverse mass (m_T) of a $p_T > 25$ GeV lepton and E_T^{miss} to select samples of $W(\rightarrow \ell\nu) + \text{jets}$ and semi-leptonic $t\bar{t}$ background events. These samples are used to estimate respectively the $W + \text{jets}$ and combined $t\bar{t}$ and single-top background populations. With the exception of SR A-loose, the CRW and CRT selections do not use the SR selection requirements applied to $\Delta\phi(\text{jet}, \mathbf{E}_T^{\text{miss}})_{\text{min}}$ or $E_T^{\text{miss}}/m_{\text{eff}}(Nj)$ ($E_T^{\text{miss}}/\sqrt{H_T}$ in SR A-medium) in order to increase CR data event statistics without significantly increasing theoretical uncertainties associated with the background estimation procedure. For the same reason the final m_{eff} (incl.) requirements are loosened to 1300 GeV in CRW and CRT for signal regions D and E-tight. Cross-checks are performed using several ‘validation region’ samples selected with requirements minimally correlated with those used in the CRs. For example, CRY estimates of the $Z(\rightarrow \nu\bar{\nu}) + \text{jets}$ background are validated with samples of $Z(\rightarrow \ell\ell) + \text{jets}$ events selected by requiring lepton pairs of opposite sign and identical flavour for which the di-lepton invariant mass lies within 25 GeV of the mass of the Z boson. The results of these cross-checks are found to be consistent with background expectations obtained from the CRs described above.

5 Analysis procedure

The observed numbers of events in the CRs for each SR are used to generate internally consistent SM background estimates for the SR via a likelihood fit. This procedure enables CR correlations due to common systematic uncertainties and contamination by other SM processes and/or SUSY signal events to be taken into account. The same fit also allows the statistical significance of the observation in the SR to be determined. Key ingredients in the fit are the ratios of expected event counts (the transfer factors TFs) from each background process between the SR and each CR, and between CRs. The TFs enable observations in the CRs to be converted into background estimates in the SR using:

$$N(\text{SR, scaled}) = N(\text{CR, obs}) \times \left[\frac{N(\text{SR, unscaled})}{N(\text{CR, unscaled})} \right], \quad (1)$$

where $N(\text{SR, scaled})$ is the estimated background contribution to the SR by a given process, $N(\text{CR, obs})$ is the observed number of data events in the CR for the process, and $N(\text{SR, unscaled})$ and $N(\text{CR, unscaled})$ are a priori estimates of the contributions from the process to the SR and CR, respectively. The ratio appearing in the square brackets in Eqn. 1 is defined to be the transfer factor TF. Similar equations containing inter-CR TFs enable the background estimates to be normalised coherently across all the CRs in a given stream.

Background estimation requires determination of the central expected values of the TFs for each SM process, together with their associated correlated and uncorrelated uncertainties. The multi-jet TFs are estimated using a data-driven technique [17], which applies a resolution function to well-measured multi-jet events in order to estimate the impact of jet energy mismeasurement and heavy-flavour semileptonic decays on E_T^{miss} and other variables. The other TF estimates use fully simulated Monte Carlo samples validated with data. Some systematic uncertainties, for instance those arising from the jet energy scale (JES), or theoretical uncertainties in MC cross-sections, largely cancel when calculating the event count ratios constituting the TFs.

The result of the likelihood fit for each SR-CR ensemble is a set of background estimates and uncertainties for the SR together with a p -value giving the probability for the hypothesis that the SR event count is compatible with background alone. However, an assumption has to be made about the migration of signal events between regions. When searching for a signal in a particular SR, first it is assumed that the signal contributes only to the SR, i.e. the signal TFs are all set to zero, giving no contribution from the signal in the CRs. If no excess is observed, then limits are set within specific SUSY model planes, taking into account the contribution of signal in the CRs and the theoretical and experimental uncertainties on the SUSY production cross-section and kinematic distributions. Exclusion limits are obtained using a likelihood test which compares the observed event rates in the signal regions with the fitted background expectation and expected signal contribution for a given model.

Monte Carlo samples are used to develop the analysis, optimise the selections, determine the transfer factors used to estimate the W -jets, Z -jets and top quark backgrounds, determine the diboson backgrounds, and to assess the sensitivity to specific SUSY signal models. The following MC generators are used:

- Samples of Z/γ^* and γ events with accompanying jets are generated with SHERPA [37] with massive b and c quarks. Theoretical uncertainties are evaluated by comparison with samples produced using ALPGEN [38].
- Samples of W events with accompanying jets are generated with ALPGEN. Theoretical uncertainties are evaluated by comparison with samples produced using SHERPA.
- Samples of top quark pair events with accompanying jets, assuming $m_{\text{top}} = 172.5$ GeV, are generated with MC@NLO [39, 40]. Theoretical uncertainties are evaluated by comparison with samples

produced using SHERPA, POWHEG [41, 42] interfaced to PYTHIA6 [43], or POWHEG interfaced to HERWIG [44, 45] using JIMMY [46] for the underlying event.

- Samples of single top quark events with accompanying jets are generated with MC@NLO [47, 48] for the s -channel and Wt processes and AcerMC [49] interfaced to PYTHIA6 for the t -channel process.
- Samples of top quark pair events with accompanying jets and a W or Z boson are generated with MADGRAPH [50, 51] and PYTHIA6.
- Samples of WZ , ZZ and $Z\gamma$ events are generated with SHERPA, while samples of WW and $W\gamma$ events are generated with ALPGEN. The samples are normalised to the Next-to-Leading Order (NLO) cross-sections obtained from MCFM [52], except for the $\nu\bar{\nu}qq$, $\ell^+\ell^-qq$, $Z\gamma$ and $W\gamma$ final states which are normalised to Leading Order (LO) cross-sections, with the resulting scale dependence ($\lesssim 25\%$) included in the theoretical uncertainties on these processes. Samples of WWW , WWZ and $WW\gamma$ events are generated with MADGRAPH and PYTHIA6, however their contribution is found to be null or negligible in all regions and hence they have not been used in the analysis.

Fragmentation and hadronisation for all ALPGEN and MC@NLO samples is performed with HERWIG, using JIMMY for the underlying event. The NLO PDF set CT10 [53] is used with SHERPA, MC@NLO and POWHEG, while the LO PDF set CTEQ6L1 [54] is used with all other generators.

SUSY signal samples are generated with HERWIG++ [55] or MadGraph/PYTHIA6 using PDF set CTEQ6L1. Signal cross-sections are calculated to next-to-leading order in the strong coupling constant, including the resummation of soft gluon emission at next-to-leading-logarithmic accuracy (NLO+NLL) [56–60].

The MC samples are generated using the same parameter set as Refs. [61–63]. Most SM background samples are passed through the ATLAS detector simulation [64] based on GEANT4 [65], while SHERPA W/Z +jets and SUSY signal samples are passed through a fast simulation using a parameterisation of the performance of the ATLAS electromagnetic and hadronic calorimeters. The fast simulation of SUSY signal events has been validated against full GEANT4 simulation for several signal model points. Differing pile-up (multiple proton-proton interactions in a given event) conditions as a function of the LHC instantaneous luminosity are taken into account by overlaying simulated minimum-bias events generated with PYTHIA8 onto the hard-scattering process and reweighting them according to the mean number of interactions expected.

6 Systematic Uncertainties

Systematic uncertainties arise through the use of the transfer factors relating observations in the control regions to background expectations in the signal regions, and from the MC modelling of minor backgrounds and the SUSY signal.

Systematic uncertainties in the background estimates are presented in Table 3. For the MC-derived transfer factors the primary common sources of systematic uncertainty are the jet energy scale (JES) calibration, jet energy resolution (JER), theoretical uncertainties, MC statistics and the reconstruction performance in the presence of pile-up. In all cases correlations between uncertainties (for instance between scale uncertainties in CRs and SRs) are taken into account where appropriate.

The JES uncertainty has been measured using the techniques described in Refs. [26, 66], leading to a slight dependence upon p_T and η . The JER uncertainty is estimated using the methods discussed in Ref. [67]. Contributions are added to both the JES and the JER uncertainties to account for the effect of pile-up at the relatively high luminosity delivered by the LHC in the 2012 run. A further uncertainty on the low- p_T calorimeter activity included in the E_T^{miss} calculation is taken into account. The combined

Signal Region	A-loose	A-medium	B-medium	B-tight	C-medium	C-tight
Total bkg	4700	122	33	2.4	210	1.6
Total bkg unc.	± 500	± 18	± 7	± 1.4	± 40	± 1.4
$\Delta\mu_{\text{Multi-jets}}$	± 0.5 [0%]	–	± 0.1 [0%]	–	–	–
$\Delta\mu_{\text{Top}}$	± 120 [3%]	± 1.6 [1%]	± 0.7 [2%]	± 0.6 [25%]	± 4 [2%]	± 0.9 [56%]
$\Delta\mu_{\text{W+jets}}$	± 110 [2%]	± 5 [4%]	± 2.0 [6%]	± 0.7 [29%]	± 6 [3%]	± 0.5 [31%]
$\Delta\mu_{\text{Z+jets}}$	± 90 [2%]	± 6 [5%]	± 2.7 [8%]	± 0.5 [21%]	± 7 [3%]	–
MC statistics	–	± 9 [7%]	± 3.1 [9%]	± 0.5 [21%]	–	± 0.4 [25%]
Jet/MET	± 50 [1%]	± 1.9 [2%]	± 1.2 [4%]	± 0.3 [13%]	± 7 [3%]	± 1.0 [63%]
Theory Z+jets	± 310 [7%]	± 8 [7%]	± 4 [12%]	± 0.1 [5%]	± 27 [13%]	–
Theory W+jets	± 230 [5%]	± 9 [7%]	± 2.6 [8%]	± 1.0 [42%]	± 17 [8%]	± 0.5 [31%]
Theory Top	± 130 [3%]	± 1.9 [2%]	± 1.3 [4%]	± 0.3 [14%]	± 10 [5%]	± 0.4 [25%]
Theory Diboson	± 190 [4%]	± 6 [5%]	± 1.9 [6%]	–	± 11 [5%]	–
Theory scales unc.	± 24 [1%]	± 0.2 [0%]	± 0.6 [2%]	± 0.1 [6%]	± 0.4 [0%]	± 0.03 [2%]
Other	± 34 [1%]	± 1.6 [1%]	± 0.2 [1%]	± 0.3 [10%]	± 0.6 [0%]	± 0.4 [25%]

Signal Region	D	E-loose	E-medium	E-tight
Total bkg	15	113	30	2.9
Total bkg unc.	± 5	± 21	± 8	± 1.8
$\Delta\mu_{\text{Multi-jets}}$	± 0.1 [1%]	± 0.1 [0%]	–	–
$\Delta\mu_{\text{Top}}$	± 0.8 [5%]	± 10 [9%]	± 3.1 [10%]	± 0.3 [11%]
$\Delta\mu_{\text{W+jets}}$	± 0.6 [4%]	± 5 [4%]	± 1.4 [5%]	± 0.2 [8%]
$\Delta\mu_{\text{Z+jets}}$	± 1.3 [9%]	± 2.2 [2%]	± 0.8 [3%]	± 0.4 [14%]
MC statistics	± 2.0 [13%]	± 8 [7%]	± 4 [13%]	± 0.7 [24%]
Jet/MET	± 0.7 [5%]	± 2.4 [2%]	± 4 [13%]	± 1.4 [48%]
Theory Z+jets	± 2.0 [13%]	± 6 [5%]	± 2.2 [7%]	± 0.3 [10%]
Theory W+jets	± 2.3 [15%]	± 4 [4%]	± 2.0 [7%]	± 0.4 [14%]
Theory Top	± 1.4 [9%]	± 15 [13%]	± 4 [13%]	± 0.5 [17%]
Theory Diboson	± 1.9 [13%]	± 2.1 [2%]	± 0.8 [3%]	–
Theory scales unc.	± 0.1 [1%]	± 0.04 [0%]	± 0.02 [0%]	± 0.03 [1%]
Other	± 0.3 [2%]	± 1.3 [1%]	± 1.0 [3%]	± 0.2 [7%]

Table 3: Breakdown of the dominant components of the systematic uncertainties on background estimates. Hyphens indicate negligible contributions. Note that components may be correlated and hence may not sum quadratically to the total background uncertainty. $\Delta\mu$ uncertainties arise from limited CR statistics and systematic uncertainties related to the CR. Uncertainties relative to the expected total background yields are listed in parenthesis.

JES, JER and E_T^{miss} uncertainty ranges from 2% of the expected background in SR E-loose to 63% in SR C-tight (where it dominates).

Uncertainties arising from theoretical models of background processes are evaluated by comparing TFs obtained from samples generated with a variety of different MC generators, as described in Section 5. In addition, the impact of uncertainties in renormalisation, factorisation and jet-parton matching scales is assessed with dedicated MC samples. The dominant such uncertainty is associated with the modelling of $W/Z+\text{jets}$ in the lower jet multiplicity signal regions (channels A–D), while in the higher jet multiplicity signal regions (channel E) the uncertainty on top quark pair production dominates. The overall largest theoretical modelling uncertainty arises from $W+\text{jet}$ production in SR B-tight (42%).

Statistical uncertainties arising from the use of finite-size MC samples range up to 25% in SR C-tight. Uncertainties arising from finite data statistics and systematics in the control regions (listed as ‘ $\Delta\mu$ ’ in Table 3) are most important for the tighter signal regions, reaching 56% for CRT in SR C-tight. The CR systematic uncertainties considered include photon and lepton reconstruction efficiency, energy scale and resolution (CRY, CRW and CRT), b -tag/veto efficiency (CRW and CRT) and photon acceptance (CRY). Uncertainties on the multi-jet transfer factors are conservatively set to 100% in all signal regions, however the small magnitude of this background in all signal regions reduces the contribution made by this uncertainty to the overall uncertainty budget. When combined with the uncertainty associated with the modelling of pile-up in MC events the resulting uncertainty (labelled ‘other’ in Table 3) is found to be less than 10% in all signal regions except SR C-tight, where its value (25%) is nevertheless smaller than the JES, MC statistics and theoretical modelling uncertainties.

Initial state radiation (ISR) can significantly affect the signal acceptance for SUSY models with small mass splittings. Systematic uncertainties arising from the treatment of ISR are studied with MC data by varying the value of α_S , renormalisation and factorisation scales, and the MadGraph/PYTHIA matching parameters. For mass splittings $\Delta m < 100$ GeV the uncertainty ranges from 25% to 45% depending on the signal region. For fixed Δm the uncertainty is found to be independent of the sparticle mass, while for fixed mass it falls approximately exponentially with increasing Δm , with a characteristic decay constant $\sim 200 - 300$ GeV.

7 Results, Interpretation and Limits

The number of events observed in the data and the number of SM events expected to enter each of the signal regions, determined using the likelihood fit, are shown in Table 4. Good agreement is observed between the data and the SM prediction, with no significant excess. The largest observed excess across the ten SRs, with a p -value for the background-only hypothesis of 0.03, occurs in SR E-loose. Predictions obtained from the likelihood fits for the numbers of events in the validation regions also agree well with the observations. Distributions of $m_{\text{eff}}(\text{incl.})$ before the final cut on this quantity for data and the different MC samples normalised with the theoretical cross-sections are shown in Figs. 1–4 for each of the channels. Examples of typical expected SUSY signals are shown for illustration. These signals correspond to the processes to which each SR is primarily sensitive – $\tilde{q}\tilde{q}$ production for the lower jet multiplicity SRs (channel A), $\tilde{q}\tilde{g}$ associated production for intermediate jet multiplicity SRs (channel B), and $\tilde{g}\tilde{g}$ production for the higher jet multiplicity SRs (channels C, D and E).

Signal Region	A-loose	A-medium	B-medium	B-tight	C-medium	C-tight
MC expected events						
Diboson	428.6	15.0	4.3	0.0	25.5	0.0
Z/ γ^* +jets	2044.4	83.1	20.6	2.3	119.4	2.6
W+jets	2109.0	58.8	16.4	2.1	88.7	1.0
$t\bar{t}$ (+EW) + single top	785.9	8.2	2.0	0.3	45.9	0.3
Fitted background events						
Diboson	430 ± 190	15 ± 7	4.3 ± 2.0	–	26 ± 11	–
Z/ γ^* +jets	1870 ± 320	57 ± 11	16 ± 5	0.2 ± 0.5	80 ± 29	$0.0^{+0.6}_{-0.0}$
W+jets	1540 ± 260	42 ± 11	10 ± 4	1.6 ± 1.2	55 ± 18	0.7 ± 0.9
$t\bar{t}$ (+EW) + single top	870 ± 180	7.8 ± 2.8	2.2 ± 2.0	0.6 ± 0.7	50 ± 11	0.9 ± 0.9
Multi-jets	33 ± 33	–	0.1 ± 0.1	–	–	–
Total bkg	4700 ± 500	122 ± 18	33 ± 7	2.4 ± 1.4	210 ± 40	1.6 ± 1.4
Observed	5333	135	29	4	228	0
$\langle\epsilon\sigma\rangle_{\text{obs}}^{95} [\text{fb}]$	66.07	2.52	0.73	0.33	4.00	0.12
S_{obs}^{95}	1341.2	51.3	14.9	6.7	81.2	2.4
S_{exp}^{95}	$1135.0^{+332.7}_{-291.5}$	$42.7^{+15.5}_{-11.4}$	$17.0^{+6.6}_{-4.6}$	$5.8^{+2.9}_{-1.8}$	$72.9^{+23.6}_{-18.0}$	$3.3^{+2.1}_{-1.2}$
$p_0(Z_n)$	0.45 (0.1)	0.27 (0.6)	0.50 (0.0)	0.34 (0.4)	0.34 (0.4)	0.50 (0.0)

Signal Region	D	E-loose	E-medium	E-tight
MC expected events				
Diboson	2.0	5.5	1.7	0.0
Z/ γ^* +jets	8.5	19.6	6.3	1.9
W+jets	4.8	23.1	5.2	0.8
$t\bar{t}$ (+EW) + single top	5.0	67.3	16.8	1.5
Fitted background events				
Diboson	2.0 ± 2.0	5.5 ± 2.1	1.7 ± 0.8	–
Z/ γ^* +jets	3.8 ± 2.5	12 ± 7	2.9 ± 2.6	0.4 ± 0.6
W+jets	3.3 ± 2.5	18 ± 7	4.9 ± 2.7	0.7 ± 0.5
$t\bar{t}$ (+EW) + single top	5.8 ± 2.1	76 ± 19	20 ± 6	1.7 ± 1.4
Multi-jets	–	1.0 ± 1.0	–	–
Total bkg	15 ± 5	113 ± 21	30 ± 8	2.9 ± 1.8
Observed	18	166	41	5
$\langle\epsilon\sigma\rangle_{\text{obs}}^{95} [\text{fb}]$	0.77	4.55	1.41	0.41
S_{obs}^{95}	15.5	92.4	28.6	8.3
S_{exp}^{95}	$13.6^{+5.1}_{-3.5}$	$57.3^{+20.0}_{-14.4}$	$21.4^{+7.6}_{-5.8}$	$6.5^{+3.0}_{-1.9}$
$p_0(Z_n)$	0.32 (0.5)	0.03 (1.9)	0.14 (1.1)	0.22 (0.8)

Table 4: Numbers of events observed in the signal regions used in the analysis ($\mathcal{L} = 20.3 \text{ fb}^{-1}$) compared with background expectations obtained from the fits described in the text. Background uncertainties include both TF systematics (see Section 6) and CR data statistical uncertainties. No signal contribution is considered in the CRs for the fit. Empty cells correspond to estimates lower than 0.1 events. Also shown are 95% CL upper limits on the visible cross-section ($\langle\epsilon\sigma\rangle_{\text{obs}}^{95}$), the visible number of signal events (S_{obs}^{95}) and the number of signal events (S_{exp}^{95}) given the expected number of background events, as well as $\pm 1\sigma$ excursions on the expectation. The p_0 -values give the probabilities of the observations being consistent with the estimated backgrounds and are constrained to ≤ 0.5 . Also presented are the equivalent Gaussian significances Z_n .

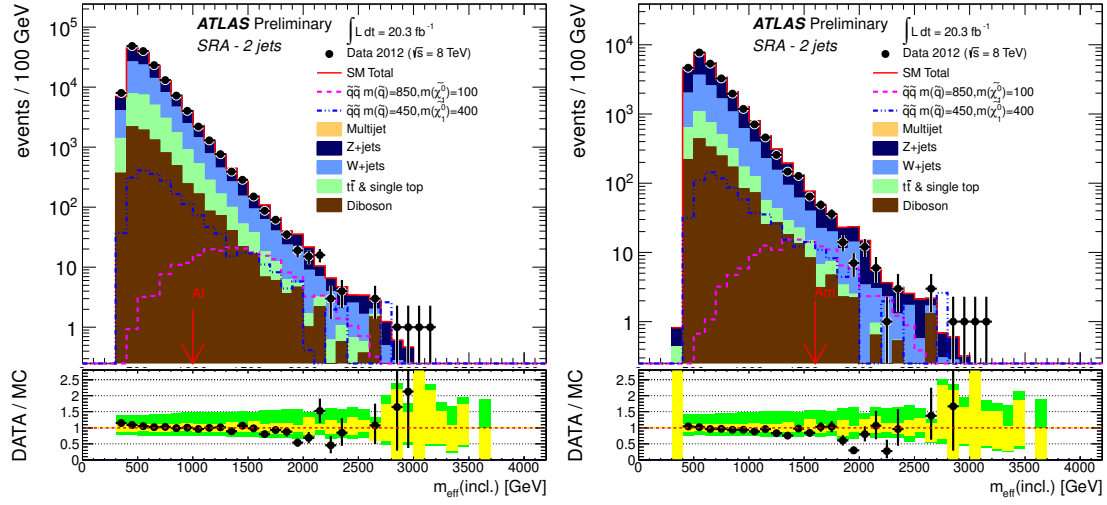


Figure 1: Observed $m_{\text{eff}}(\text{incl.})$ distributions for channel A for ‘loose’ (left) and ‘medium’ (right) selection criteria. With the exception of the multi-jet background (which is estimated using the data-driven technique described in the text), the histograms denote the MC background expectations, normalised to cross-section times integrated luminosity. In the lower panels the yellow error bands denote the experimental and MC statistical uncertainties, while the green bands show the total uncertainty. The red arrows indicate the values at which the requirements on $m_{\text{eff}}(\text{incl.})$ are applied. Expected distributions for two benchmark model points characterised by $\tilde{q}\tilde{q}$ production are also shown for comparison (masses in GeV).

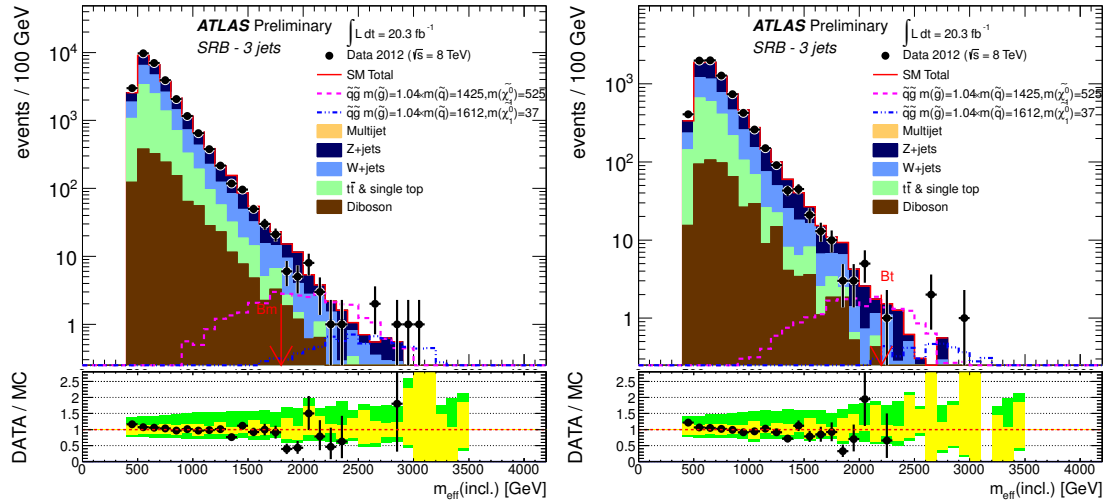


Figure 2: Observed $m_{\text{eff}}(\text{incl.})$ distributions for channel B for ‘medium’ (left) and ‘tight’ (right) selection criteria. With the exception of the multi-jet background (which is estimated using the data-driven technique described in the text), the histograms denote the MC background expectations, normalised to cross-section times integrated luminosity. In the lower panels the yellow error bands denote the experimental and MC statistical uncertainties, while the green bands show the total uncertainty. The red arrows indicate the values at which the requirements on $m_{\text{eff}}(\text{incl.})$ are applied. Expected distributions for two benchmark model points characterised by $\tilde{q}\tilde{g}$ production are also shown for comparison (masses in GeV).

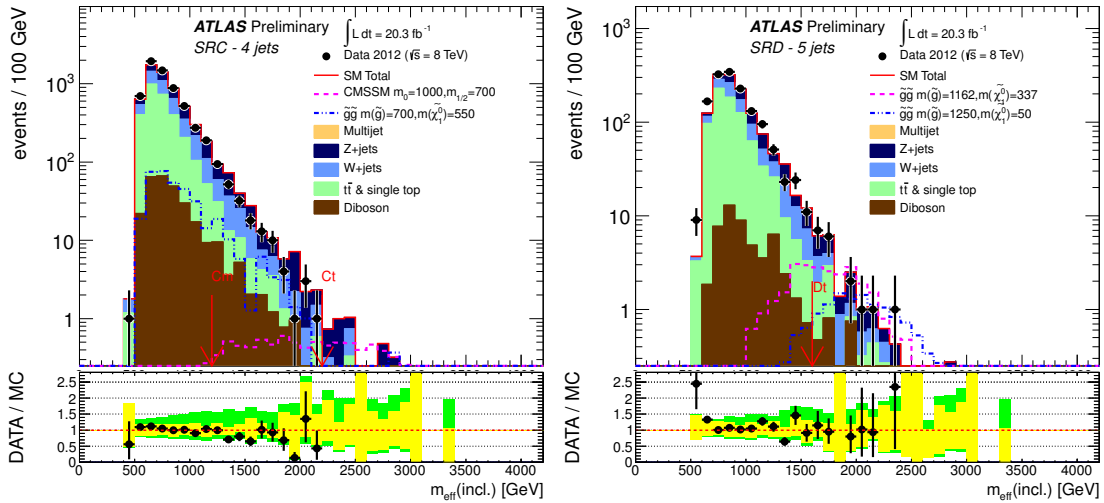


Figure 3: Observed $m_{\text{eff}}(\text{incl.})$ distributions for channels C (left) and D (right). With the exception of the multi-jet background (which is estimated using the data-driven technique described in the text), the histograms denote the MC background expectations, normalised to cross-section times integrated luminosity. In the lower panels the yellow error bands denote the experimental and MC statistical uncertainties, while the green bands show the total uncertainty. The red arrows indicate the values at which the requirements on $m_{\text{eff}}(\text{incl.})$ are applied. Expected distributions for two benchmark model points are also shown for comparison (masses in GeV).

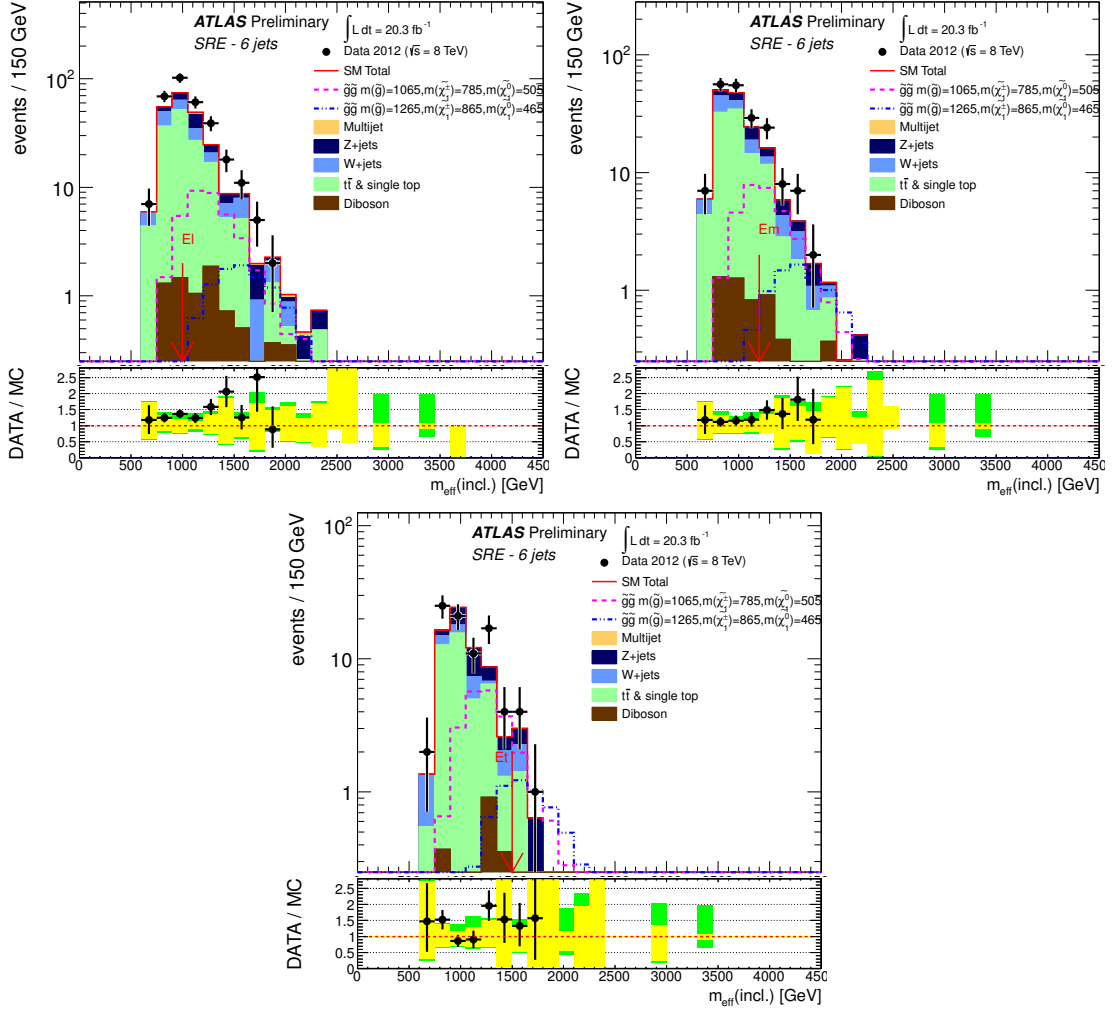


Figure 4: Observed $m_{\text{eff}}(\text{incl.})$ distributions for channel E for ‘loose’ (top left), ‘medium’ (top right) and ‘tight’ (bottom) selection criteria. With the exception of the multi-jet background (which is estimated using the data-driven technique described in the text), the histograms denote the MC background expectations, normalised to cross-section times integrated luminosity. In the lower panels the yellow error bands denote the experimental and MC statistical uncertainties, while the green bands show the total uncertainty. The red arrows indicate the values at which the requirements on $m_{\text{eff}}(\text{incl.})$ are applied. Expected distributions for two benchmark model points characterised by $\tilde{g}\tilde{g}$ production are also shown for comparison (masses in GeV).

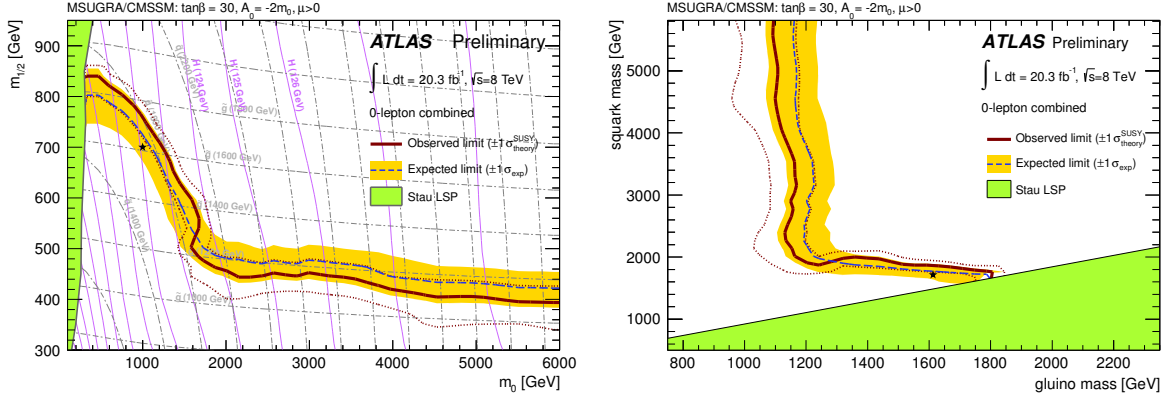


Figure 5: Exclusion limits for MSUGRA/CMSSM models with $\tan\beta = 30$, $A_0 = -2m_0$ and $\mu > 0$ presented (left) in the m_0 – $m_{1/2}$ plane and (right) in the $m_{\tilde{g}}$ – $m_{\tilde{q}}$ plane. Exclusion limits are obtained by using the signal region with the best expected sensitivity at each point. The blue dashed lines show the expected limits at 95% CL, with the light (yellow) bands indicating the 1σ excursions due to experimental and background-theory uncertainties. Observed limits are indicated by medium (maroon) curves, where the solid contour represents the nominal limit, and the dotted lines are obtained by varying the signal cross-section by the theoretical scale and PDF uncertainties. The black star indicates the MSUGRA/CMSSM benchmark model used in Fig. 3(left).

In the absence of a statistically significant excess limits are set on contributions to the SRs from new physics. Model independent limits are listed in Table 4 for the number of new physics events and the visible cross-section σ_{vis} (defined as the product of the production cross-section times reconstruction efficiency times acceptance), computed assuming an absence of signal in the control regions.

Data from all the channels are used to set limits on SUSY models, taking the SR with the best expected sensitivity at each point in several parameter spaces. A profile log-likelihood ratio test in combination with the CL_s prescription [68] is used to derive 95% CL exclusion regions. The nominal signal cross-section and the uncertainty are taken from an ensemble of cross-section predictions using different PDF sets and factorisation and renormalisation scales, as described in Ref. [69]. Observed limits are calculated for both the nominal cross-section, and $\pm 1\sigma$ uncertainties. Numbers quoted in the text are evaluated from the observed exclusion limit based on the nominal cross-section less one sigma on the theoretical uncertainty.

In Fig. 5 the results are interpreted in the $\tan\beta = 30$, $A_0 = -2m_0$, $\mu > 0$ slice of MSUGRA/CMSSM models ². The best performing signal regions are E-tight for $m_0 \gtrsim 1500$ GeV and C-tight for $m_0 \lesssim 1500$ GeV. Results are presented in both the m_0 – $m_{1/2}$ and $m_{\tilde{g}}$ – $m_{\tilde{q}}$ planes. The sparticle mass spectra and decay tables are calculated with SUSY-HIT [70] interfaced to the SOFTSUSY spectrum generator [71] and SDECAY [72].

An interpretation of the results is also presented in Fig. 6 as a 95% CL exclusion region in the $(m_{\tilde{g}}, m_{\tilde{q}})$ -plane for a simplified set of phenomenological MSSM (Minimal Supersymmetric extension of the SM) models with $m_{\tilde{\chi}_1^0}$ equal to 0, 395 GeV or 695 GeV. In these models the gluino mass and the masses of the ‘light’-flavour squarks (of the first two generations, including both \tilde{q}_R and \tilde{q}_L , and assuming mass degeneracy) are set to the values shown on the axes of the figure. All other supersymmetric particles, including the squarks of the third generation, are decoupled.

²Five parameters are needed to specify a particular MSUGRA/CMSSM model: the universal scalar mass, m_0 , the universal gaugino mass $m_{1/2}$, the universal trilinear scalar coupling, A_0 , the ratio of the vacuum expectation values of the two Higgs fields, $\tan\beta$, and the sign of the higgsino mass parameter, $\mu = \pm$.

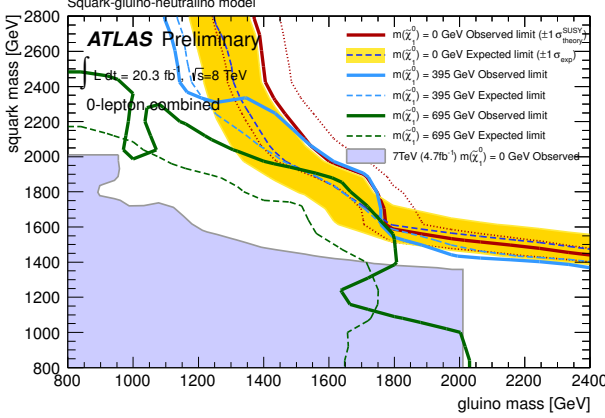


Figure 6: Exclusion limits for a simplified phenomenological MSSM scenario with only strong production of gluinos and first- and second-generation squarks (of common mass), with direct decays to jets and lightest neutralinos. Three values of the lightest neutralino mass are considered: $m_{\tilde{\chi}_1^0} = 0, 395$ and 695 GeV. Exclusion limits are obtained by using the signal region with the best expected sensitivity at each point. The dashed lines show the expected limits at 95% CL, with the light (yellow) band indicating the 1σ experimental and background-theory uncertainties on the $m_{\tilde{\chi}_1^0} = 0$ limit. Observed limits are indicated by solid curves. The dotted lines represent the $m_{\tilde{\chi}_1^0} = 0$ observed limits obtained by varying the signal cross-section by the theoretical scale and PDF uncertainties. Previous results for $m_{\tilde{\chi}_1^0} = 0$ from ATLAS at 7 TeV [17] are represented by the shaded (light blue) area. Results at 7 TeV are valid for squark or gluino masses below 2000 GeV, the mass range studied for that analysis.

In Fig. 7 limits are shown for three classes of simplified model in which only direct production of (a) gluino pairs, (b) light-flavour squarks and gluinos or (c) light-flavour squark pairs is kinematically possible, with all other superpartners, except for the neutralino LSP, decoupled. This forces each light-flavour squark or gluino to decay directly to jets and an LSP. Cross-sections are evaluated assuming decoupled light-flavour squarks or gluinos in cases (a) and (c), respectively. In all cases squarks of the third generation are decoupled. In case (b) the masses of the light-flavour squarks are set to 0.96 times the mass of the gluino. The expected limits for case (c) do not extend substantially beyond those obtained from the previous published ATLAS analysis [17] because the events closely resemble the predominant $W/Z + 2\text{-jet}$ background, leading the background uncertainties to be dominated by systematics.

In Fig. 8 limits are shown for pair produced gluinos each decaying via an intermediate $\tilde{\chi}_1^\pm$ to two quarks, a W boson and a $\tilde{\chi}_1^0$, and pair produced light squarks each decaying via an intermediate $\tilde{\chi}_1^\pm$ to a quark, a W boson and a $\tilde{\chi}_1^0$. Results are presented for models in which either the $\tilde{\chi}_1^0$ mass is fixed to 60 GeV, or the mass splitting between the $\tilde{\chi}_1^\pm$ and the $\tilde{\chi}_1^0$, relative to that between the squark or gluino and the $\tilde{\chi}_1^0$, is fixed to 0.5.

In Fig. 9 the results are interpreted in the context of a Non-Universal Higgs Mass model with gaugino mediation (NUHMG) [73] with parameters $\tan\beta = 10$, $\mu > 0$, $m_{H_2}^2 = 0$, and A_0 chosen to maximize the mass of the lightest Higgs boson. The two remaining free parameters of the model $m_{1/2}$ and $m_{H_1}^2$ are chosen such that the next-to-lightest SUSY particle (NLSP) is a tau-sneutrino with properties satisfying Big Bang Nucleosynthesis constraints.

In Fig. 10(left) limits are presented for a simplified phenomenological SUSY model in which pairs of gluinos are produced, each of which then decays to a top squark and a top quark, with the top squark decaying to a charm quark and $\tilde{\chi}_1^0$.

In addition to these interpretations in terms of SUSY models, an alternative interpretation in the context of the minimal universal extra dimension (mUED) model [75] with similar phenomenological

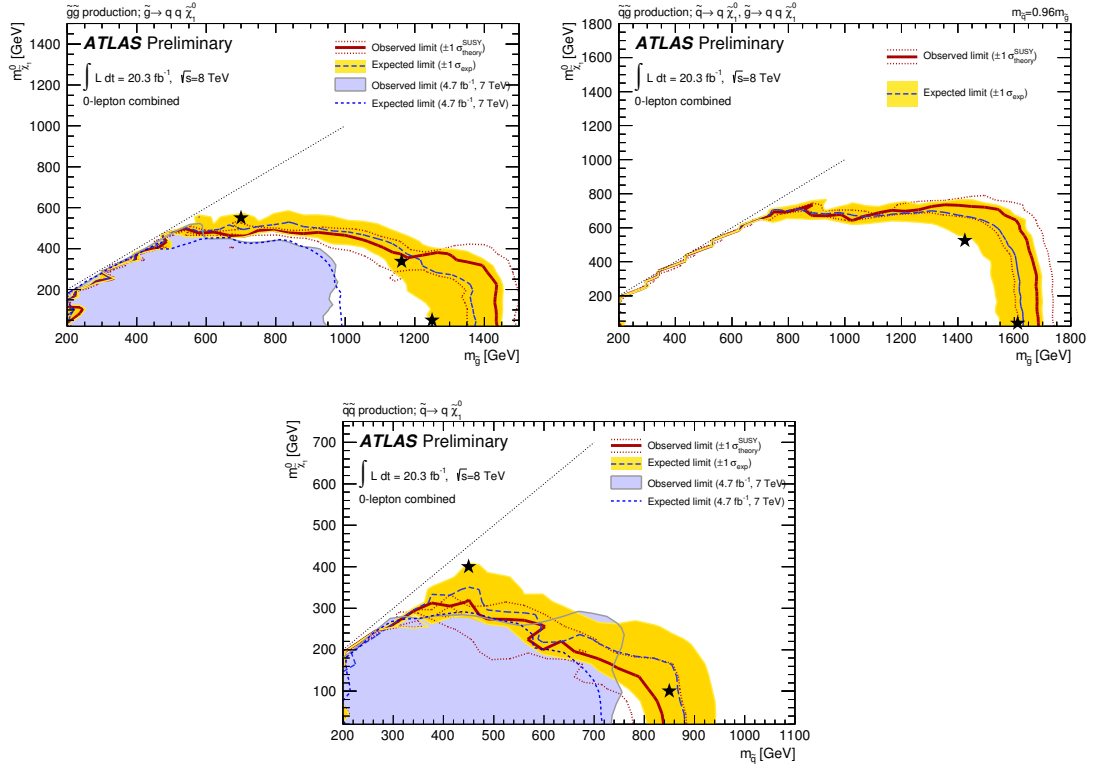


Figure 7: Exclusion limits for direct production of (case a – top left) gluino pairs with decoupled squarks, (case b – top right) light-flavour squarks and gluinos and (case c – bottom) light-flavour squark pairs with decoupled gluinos. Gluinos (light-flavour squarks) are required to decay to two jets (one jet) and a neutralino LSP. Exclusion limits are obtained by using the signal region with the best expected sensitivity at each point. The blue dashed lines show the expected limits at 95% CL, with the light (yellow) bands indicating the 1σ excursions due to experimental and background-theory uncertainties. Observed limits are indicated by medium (maroon) curves, where the solid contour represents the nominal limit, and the dotted lines are obtained by varying the signal cross-section by the theoretical scale and PDF uncertainties. Previous results from ATLAS [17] are represented by the shaded (light blue) areas and light blue dotted lines. The black stars indicate the benchmark models used in Figs. 1–4.

properties to R-parity conserving SUSY is also presented in Fig. 10(right). This scenario is the minimal extension of the SM with one additional spatial dimension. The properties of the model are fully determined by three parameters: the compactification radius of the extra dimension R , the cut-off scale Λ and the Higgs boson mass m_h . In this analysis the Higgs boson mass is fixed to 125 GeV while R and Λ are treated as free parameters. $1/R$ sets the mass scale of the new Kaluza-Klein (KK) particles predicted by the model while $\Lambda \cdot R$ is related to the degree of compression of the KK-particle mass spectrum: models with small values of $\Lambda \cdot R$ possess small mass splittings between KK-particle states and vice versa. Exclusion limits are set in the $1/R$ versus $\Lambda \cdot R$ plane.

In the CMSSM/MSUGRA case, the limit on $m_{1/2}$ is greater than 340 GeV for $m_0 < 6$ TeV and reaches 800 GeV for low values of m_0 . Equal mass light-flavour squarks and gluinos are excluded below 1700 GeV in this scenario. A limit of 1700 GeV for equal mass light-flavour squarks and gluinos is found for the simplified MSSM scenario with a massless lightest neutralino shown in Fig. 6. In the simplified model cases of Fig. 7 (a) and (c), when the lightest neutralino is massless the limit on the gluino mass (case (a)) is 1350 GeV, and that on the light-flavour squark mass (case (c)) is 780 GeV.

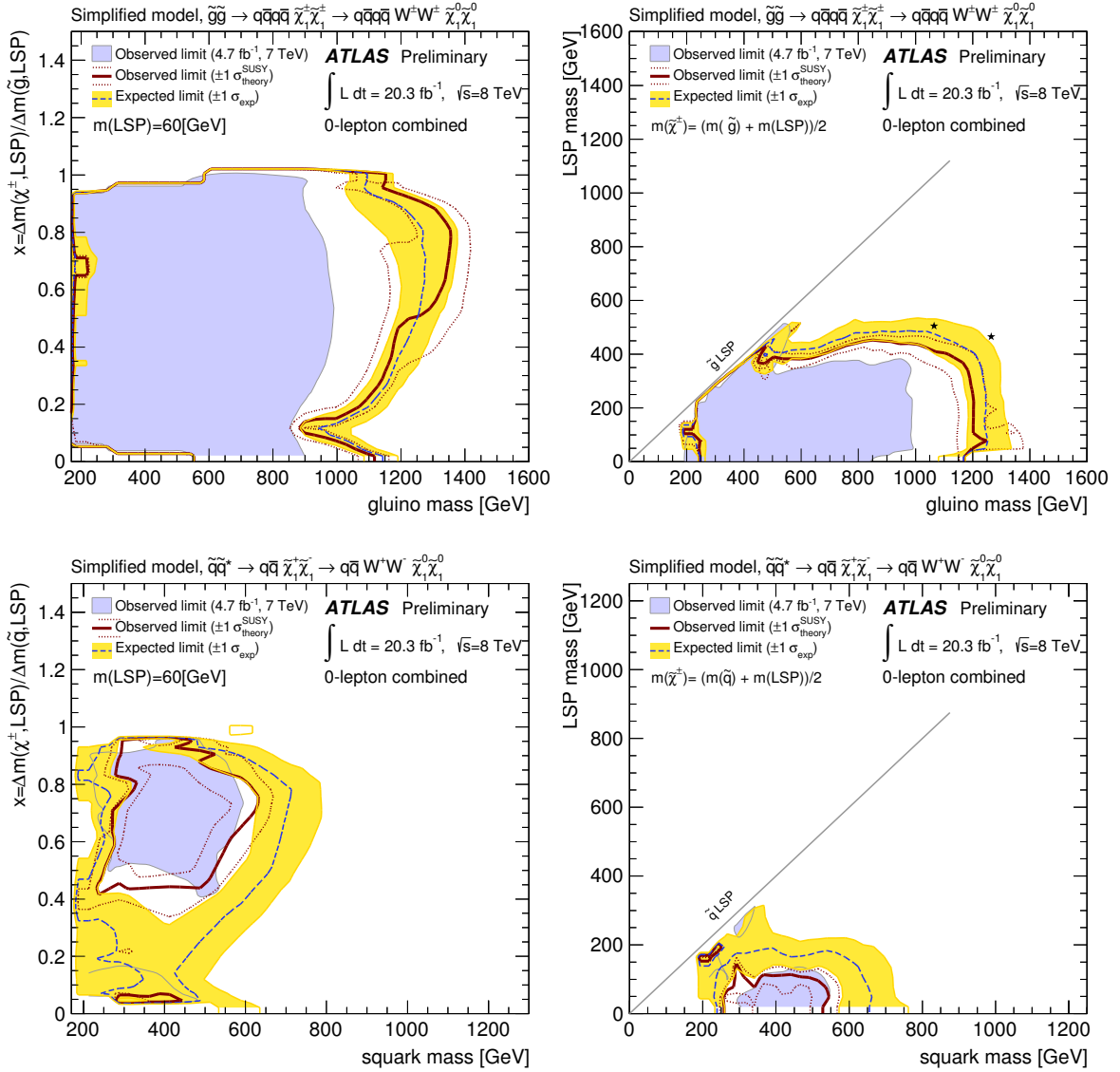


Figure 8: Exclusion limits for pair produced gluinos each decaying via an intermediate $\tilde{\chi}_1^\pm$ to two quarks, a W boson and a $\tilde{\chi}_1^0$ (top) or pair produced light squarks each decaying via an intermediate $\tilde{\chi}_1^\pm$ to a quark, a W boson and a $\tilde{\chi}_1^0$ (bottom). The left-hand figures show results for models with fixed $m(\tilde{\chi}_1^0) = 60$ GeV and varying values of $x = (m_{\tilde{\chi}_1^\pm} - m_{\tilde{\chi}_1^0}) / (m_{\tilde{g}} - m_{\tilde{\chi}_1^0})$, where $y = \tilde{g}(y = \tilde{q})$ for the top(bottom) figure. The right-hand plots show results for models with a fixed value of $x = 1/2$ and varying values of $m_{\tilde{\chi}_1^0}$. Exclusion limits are obtained by using the signal region with the best expected sensitivity at each point. The blue dashed lines show the expected limits at 95% CL, with the light (yellow) bands indicating the 1σ excursions due to experimental and background-theory uncertainties. Observed limits are indicated by medium (maroon) curves, where the solid contour represents the nominal limit, and the dotted lines are obtained by varying the signal cross-section by the theoretical scale and PDF uncertainties. Previous results from ATLAS [17] are represented by the shaded (light blue) areas.

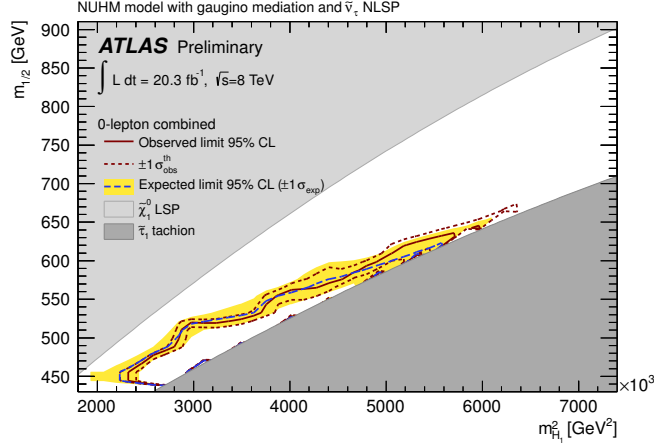


Figure 9: Exclusion limits in the $m_{1/2}$ versus $m_{H_1}^2$ plane for the NUHMG model described in the text. Exclusion limits are obtained by using the signal region with the best expected sensitivity at each point. The blue dashed lines show the expected limits at 95% CL, with the light (yellow) bands indicating the 1σ excursions due to experimental and background-theory uncertainties. Observed limits are indicated by medium (maroon) curves, where the solid contour represents the nominal limit, and the dotted lines are obtained by varying the signal cross-section by the theoretical scale and PDF uncertainties.

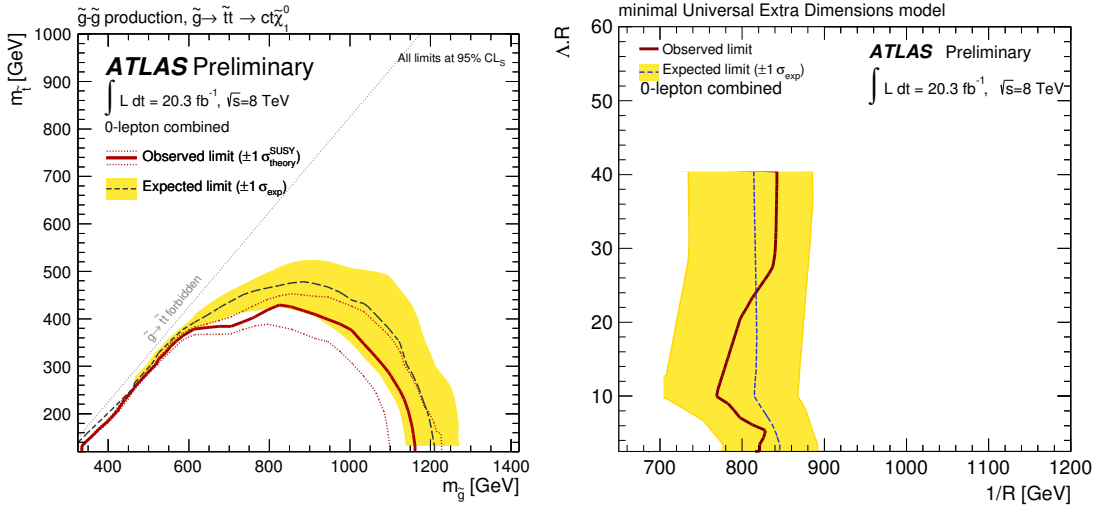


Figure 10: Exclusion limits for pair produced gluinos each decaying into a \tilde{t} and a $\tilde{\chi}_1^0$, with the subsequent decay $\tilde{t} \rightarrow c\tilde{\chi}_1^0$ and $\Delta M(\tilde{t}, \tilde{\chi}_1^0) = 20$ GeV (left), and in the $1/R$ versus $\Lambda \cdot R$ plane for the mUED model described in the text (right). Exclusion limits are obtained by using the signal region with the best expected sensitivity at each point. The blue dashed lines show the expected limits at 95% CL, with the light (yellow) bands indicating the 1σ excursions due to experimental and background-theory uncertainties. Observed limits are indicated by medium (maroon) curves, where the solid contour represents the nominal limit. In the left-hand figure the dotted lines are obtained by varying the signal cross-section by the theoretical scale and PDF uncertainties. In the right-hand figure theoretical uncertainties are not available. Models with $1/R \lesssim 650$ GeV are excluded by previous analyses as described in Ref. [74].

8 Summary

This note reported a search for new physics in final states containing high- p_T jets, large missing transverse momentum and no electrons or muons, based on a 20.3 fb^{-1} dataset recorded by the ATLAS experiment at the LHC in 2012. Good agreement was seen between the numbers of events observed in the data and the numbers of events expected from SM processes.

Results were presented for a variety of SUSY models and for a specific model of extra dimensions. In particular the results were interpreted in terms of MSUGRA/CMSSM models with $\tan\beta = 30$, $A_0 = -2m_0$ and $\mu > 0$, and in terms of simplified models with only light-flavour squarks, or gluinos, or both, together with a neutralino LSP, with the other SUSY particles decoupled. In the MSUGRA/CMSSM models, values of $m_{1/2} < 340 \text{ GeV}$ are excluded at the 95% confidence level for $m_0 < 6 \text{ TeV}$ and $m_{1/2} < 800 \text{ GeV}$ for low m_0 . Equal mass squarks and gluinos are excluded below 1700 GeV in this scenario. A limit of 1700 GeV for equal mass light-flavour squarks and gluinos was found for simplified MSSM models with a massless lightest neutralino. For a massless lightest neutralino, gluino masses below 1350 GeV are excluded at the 95% confidence level in a simplified model with only gluinos and the lightest neutralino. For a simplified model involving the strong production of squarks of the first two generations, with decays to a massless lightest neutralino, squark masses below 780 GeV are excluded.

References

- [1] L. Evans and P. Bryant, *LHC Machine*, JINST **3** (2008) S08001.
- [2] H. Miyazawa, *Baryon Number Changing Currents*, Prog. Theor. Phys. **36** (6) (1966) 1266–1276.
- [3] P. Ramond, *Dual Theory for Free Fermions*, Phys. Rev. **D3** (1971) 2415–2418.
- [4] Y. A. Golfand and E. P. Likhtman, *Extension of the Algebra of Poincare Group Generators and Violation of p Invariance*, JETP Lett. **13** (1971) 323–326. [Pisma Zh. Eksp. Teor. Fiz. 13 (1971) 452–455].
- [5] A. Neveu and J. H. Schwarz, *Factorizable dual model of pions*, Nucl. Phys. **B31** (1971) 86–112.
- [6] A. Neveu and J. H. Schwarz, *Quark Model of Dual Pions*, Phys. Rev. **D4** (1971) 1109–1111.
- [7] J. Gervais and B. Sakita, *Field theory interpretation of supergauges in dual models*, Nucl. Phys. **B34** (1971) 632–639.
- [8] D. V. Volkov and V. P. Akulov, *Is the Neutrino a Goldstone Particle?*, Phys. Lett. **B46** (1973) 109–110.
- [9] J. Wess and B. Zumino, *A Lagrangian Model Invariant Under Supergauge Transformations*, Phys. Lett. **B49** (1974) 52.
- [10] J. Wess and B. Zumino, *Supergauge Transformations in Four-Dimensions*, Nucl. Phys. **B70** (1974) 39–50.
- [11] P. Fayet, *Supersymmetry and Weak, Electromagnetic and Strong Interactions*, Phys. Lett. **B64** (1976) 159.
- [12] P. Fayet, *Spontaneously Broken Supersymmetric Theories of Weak, Electromagnetic and Strong Interactions*, Phys. Lett. **B69** (1977) 489.

- [13] G. R. Farrar and P. Fayet, *Phenomenology of the Production, Decay, and Detection of New Hadronic States Associated with Supersymmetry*, Phys. Lett. **B76** (1978) 575–579.
- [14] P. Fayet, *Relations Between the Masses of the Superpartners of Leptons and Quarks, the Goldstino Couplings and the Neutral Currents*, Phys. Lett. **B84** (1979) 416.
- [15] S. Dimopoulos and H. Georgi, *Softly Broken Supersymmetry and SU(5)*, Nucl. Phys. **B193** (1981) 150.
- [16] ATLAS Collaboration, *Search for squarks and gluinos with the ATLAS detector using final states with jets and missing transverse momentum at $\sqrt{s} = 8$ TeV*, ATLAS-CONF-2012-109, <http://cds.cern.ch/record/1472710>.
- [17] ATLAS Collaboration, *Search for squarks and gluinos with the ATLAS detector in final states with jets and missing transverse momentum using 4.7 fb^{-1} of $\sqrt{s} = 7$ TeV proton-proton collision data*, Phys. Rev. **D87** (2013) 012008, [arXiv:1208.0949 \[hep-ex\]](https://arxiv.org/abs/1208.0949).
- [18] ATLAS Collaboration, *Search for squarks and gluinos using final states with jets and missing transverse momentum with the ATLAS detector in $\sqrt{s} = 7$ TeV proton-proton collisions*, Phys. Lett. **B710** (2012) 67–85, [arXiv:1109.6572 \[hep-ex\]](https://arxiv.org/abs/1109.6572).
- [19] ATLAS Collaboration, *Search for squarks and gluinos using final states with jets and missing transverse momentum with the ATLAS detector in $\sqrt{s} = 7$ TeV proton-proton collisions*, Phys. Lett. **B701** (2011) 186–203, [arXiv:1102.5290 \[hep-ex\]](https://arxiv.org/abs/1102.5290).
- [20] ATLAS Collaboration, *Search for supersymmetry at $\sqrt{s} = 8$ TeV in final states with jets, missing transverse momentum and one isolated lepton*, ATLAS-CONF-2012-104. <http://cds.cern.ch/record/1472673>.
- [21] ATLAS Collaboration, *Search for supersymmetry in final states with jets, missing transverse momentum and one isolated lepton in $\sqrt{s} = 7$ TeV pp collisions using 1 fb^{-1} of ATLAS data*, Phys. Rev. **D85** (2012) 012006, [arXiv:1109.6606 \[hep-ex\]](https://arxiv.org/abs/1109.6606).
- [22] ATLAS Collaboration, *The ATLAS Experiment at the CERN Large Hadron Collider*, 2008. JINST **3** (2008) S08003.
- [23] ATLAS Collaboration, *Improved luminosity determination in pp collisions at $\sqrt{s} = 7$ TeV using the ATLAS detector at the LHC*, [arXiv:1302.4393 \[hep-ex\]](https://arxiv.org/abs/1302.4393).
- [24] M. Cacciari, G. P. Salam, and G. Soyez, *The anti- k_t jet clustering algorithm*, JHEP **04** (2008) 063, [arXiv:0802.1189 \[hep-ph\]](https://arxiv.org/abs/0802.1189).
- [25] M. Cacciari and G. P. Salam, *Dispelling the N^3 myth for the k_t jet-finder*, Phys. Lett. **B641** (2006) 57–61, [arXiv:hep-ph/0512210](https://arxiv.org/abs/hep-ph/0512210).
- [26] ATLAS Collaboration, *Jet energy measurement with the ATLAS detector in proton-proton collisions at $\sqrt{s} = 7$ TeV*, [arXiv:1112.6426 \[hep-ex\]](https://arxiv.org/abs/1112.6426).
- [27] W. Lampl et al., *Calorimeter Clustering Algorithms: Description and Performance*, ATL-LARG-PUB-2008-002. <http://cdsweb.cern.ch/record/1099735>.
- [28] M. Cacciari and G. P. Salam, *Pileup subtraction using jet areas*, Phys. Lett. **B659** (2008) 119–126, [arXiv:0707.1378 \[hep-ph\]](https://arxiv.org/abs/0707.1378).

[29] C. Issever, K. Borras, and D. Wegener, *An improved weighting algorithm to achieve software compensation in a fine grained LAr calorimeter*, Nucl.Instrum.Meth. **A545** (2005) 803–812, [arXiv:physics/0408129](https://arxiv.org/abs/physics/0408129) [physics].

[30] *Measurement of the b-tag Efficiency in a Sample of Jets Containing Muons with 5 fb^{-1} of Data from the ATLAS Detector*, ATLAS-CONF-2012-043. <http://cdsweb.cern.ch/record/1435197>.

[31] ATLAS Collaboration, *Electron performance measurements with the ATLAS detector using the 2010 LHC proton-proton collision data*, Eur. Phys. J. **C72** (2012) 1909, [arXiv:1110.3174](https://arxiv.org/abs/1110.3174) [hep-ex].

[32] ATLAS Collaboration, *Muon Momentum Resolution in First Pass Reconstruction of pp Collision Data Recorded by ATLAS in 2010*, ATLAS-CONF-2011-046. <http://cdsweb.cern.ch/record/1338575>.

[33] ATLAS Collaboration, *Muon reconstruction efficiency in reprocessed 2010 LHC proton-proton collision data recorded with the ATLAS detector*, ATLAS-CONF-2011-063. <http://cdsweb.cern.ch/record/1345743>.

[34] ATLAS Collaboration, *Measurements of the photon identification efficiency with the ATLAS detector using 4.9 fb^{-1} of pp collision data collected in 2011*, ATLAS-CONF-2012-123. <https://cds.cern.ch/record/1473426>.

[35] ATLAS Collaboration, *Performance of Missing Transverse Momentum Reconstruction in Proton-Proton Collisions at 7 TeV with ATLAS*, Eur.Phys.J. **C72** (2012) 1844, [arXiv:1108.5602](https://arxiv.org/abs/1108.5602) [hep-ex].

[36] *Selection of jets produced in proton-proton collisions with the ATLAS detector using 2011 data*, ATLAS-CONF-2012-020. <http://cdsweb.cern.ch/record/1430034>.

[37] T. Gleisberg et al., *Event generation with SHERPA 1.1*, JHEP **0902** (2009) 007, [arXiv:0811.4622](https://arxiv.org/abs/0811.4622) [hep-ph].

[38] M. L. Mangano, M. Moretti, F. Piccinini, R. Pittau, and A. D. Polosa, *ALPGEN, a generator for hard multiparton processes in hadronic collisions*, JHEP **07** (2003) 001, [arXiv:hep-ph/0206293](https://arxiv.org/abs/hep-ph/0206293).

[39] S. Frixione and B. R. Webber, *Matching NLO QCD computations and parton shower simulations*, JHEP **06** (2002) 029, [arXiv:hep-ph/0204244](https://arxiv.org/abs/hep-ph/0204244).

[40] S. Frixione, P. Nason, and B. R. Webber, *Matching NLO QCD and parton showers in heavy flavour production*, JHEP **08** (2003) 007, [arXiv:hep-ph/0305252](https://arxiv.org/abs/hep-ph/0305252).

[41] P. Nason, *A New method for combining NLO QCD with shower Monte Carlo algorithms*, JHEP **0411** (2004) 040, [arXiv:hep-ph/0409146](https://arxiv.org/abs/hep-ph/0409146) [hep-ph].

[42] S. Frixione, P. Nason, and C. Oleari, *Matching NLO QCD computations with parton shower simulations: the POWHEG method*, JHEP **0711** (2007) 070, [arXiv:0709.2092](https://arxiv.org/abs/0709.2092) [hep-ph].

[43] T. Sjostrand, S. Mrenna, and P. Z. Skands, *PYTHIA 6.4 Physics and Manual*, JHEP **0605** (2006) 026, [arXiv:hep-ph/0603175](https://arxiv.org/abs/hep-ph/0603175).

[44] G. Corcella et al., *HERWIG 6.5: an event generator for Hadron Emission Reactions With Interfering Gluons (including supersymmetric processes)*, JHEP **01** (2001) 010, arXiv:hep-ph/0011363.

[45] G. Corcella et al., *HERWIG 6.5 release note*, 2002. arXiv:hep-ph/0210213.

[46] J. M. Butterworth, J. R. Forshaw, and M. H. Seymour, *Multiparton interactions in photoproduction at HERA*, Z. Phys. **C72** (1996) 637–646, arXiv:hep-ph/9601371.

[47] S. Frixione, E. Laenen, P. Motylinski, and B. R. Webber, *Single-top production in MC@NLO*, JHEP **03** (2006) 092, arXiv:hep-ph/0512250.

[48] S. Frixione, E. Laenen, P. Motylinski, B. R. Webber, and C. D. White, *Single-top hadroproduction in association with a W boson*, JHEP **07** (2008) 029, arXiv:0805.3067 [hep-ph].

[49] B. P. Kersevan and E. Richter-Was, *The Monte Carlo event generator AcerMC version 2.0 with interfaces to PYTHIA 6.2 and HERWIG 6.5*, arXiv:hep-ph/0405247 [hep-ph].

[50] J. Alwall et al., *MadGraph/MadEvent v4: The New Web Generation*, JHEP **09** (2007) 028, arXiv:0706.2334 [hep-ph].

[51] F. Maltoni and T. Stelzer, *MadEvent: Automatic event generation with MadGraph*, JHEP **0302** (2003) 027, arXiv:hep-ph/0208156 [hep-ph].

[52] J. M. Campbell, R. K. Ellis, and C. Williams, *Vector boson pair production at the LHC*, JHEP **1107** (2011) 018, arXiv:1105.0020 [hep-ph].

[53] H.-L. Lai et al., *New parton distributions for collider physics*, Phys. Rev. **D82** (2010) 074024, arXiv:1007.2241 [hep-ph].

[54] J. Pumplin et al., *New generation of parton distributions with uncertainties from global QCD analysis*, JHEP **0207** (2002) 012, arXiv:hep-ph/0201195 [hep-ph].

[55] M. Bahr et al., *Herwig++ Physics and Manual*, Eur. Phys. J. **C58** (2008) 639–707, arXiv:0803.0883 [hep-ph].

[56] W. Beenakker, R. Hopker, M. Spira, and P. M. Zerwas, *Squark and gluino production at hadron colliders*, Nucl. Phys. **B492** (1997) 51–103, arXiv:hep-ph/9610490.

[57] A. Kulesza and L. Motyka, *Threshold resummation for squark-antisquark and gluino-pair production at the LHC*, Phys. Rev. Lett. **102** (2009) 111802, arXiv:0807.2405 [hep-ph].

[58] A. Kulesza and L. Motyka, *Soft gluon resummation for the production of gluino-gluino and squark-antisquark pairs at the LHC*, Phys. Rev. **D80** (2009) 095004, arXiv:0905.4749 [hep-ph].

[59] W. Beenakker et al., *Soft-gluon resummation for squark and gluino hadroproduction*, JHEP **0912** (2009) 041, arXiv:0909.4418 [hep-ph].

[60] W. Beenakker et al., *Squark and gluino hadroproduction*, Int. J. Mod. Phys. **A26** (2011) 2637–2664, arXiv:1105.1110 [hep-ph].

[61] ATLAS Collaboration, *ATLAS tunes of PYTHIA 6 and Pythia 8 for MC11*, ATL-PHYS-PUB-2011-009. <http://cdsweb.cern.ch/record/1363300>.

[62] ATLAS Collaboration, *Further ATLAS tunes of PYTHIA6 and Pythia 8*, ATL-PHYS-PUB-2011-014. <http://cdsweb.cern.ch/record/1400677>.

[63] ATLAS Collaboration, *First tuning of HERWIG/JIMMY to ATLAS data*, ATL-PHYS-PUB-2010-014. <http://cdsweb.cern.ch/record/1303025>.

[64] ATLAS Collaboration, *The ATLAS Simulation Infrastructure*, Eur. Phys. J. **C70** (2010) 823, arXiv:1005.4568 [physics.ins-det].

[65] GEANT4 Collaboration, S. Agostinelli et al., *GEANT4: A simulation toolkit*, Nucl. Instrum. Meth. **A506** (2003) 250–303.

[66] ATLAS Collaboration, *Single hadron response measurement and calorimeter jet energy scale uncertainty with the ATLAS detector at the LHC*, arXiv:1203.1302 [hep-ex].

[67] ATLAS Collaboration, *Jet energy resolution and selection efficiency relative to track jets from in-situ techniques with the ATLAS Detector Using Proton-Proton Collisions at a Center of Mass Energy $\sqrt{s} = 7$ TeV*, ATLAS-CONF-2010-054. <https://cdsweb.cern.ch/record/1281311>.

[68] A. Read, *Presentation of search results: the CLs technique*, Journal of Physics G: Nucl. Part. Phys. **28** (2002) 2693–2704.

[69] M. Kramer et al., *Supersymmetry production cross sections in pp collisions at $\sqrt{s} = 7$ TeV*, arXiv:1206.2892 [hep-ph].

[70] A. Djouadi, M. Muhlleitner, and M. Spira, *Decays of supersymmetric particles: The Program SUSY-HIT (SUspect-SdecaY-Hdecay-Interface)*, Acta Phys. Polon. **B38** (2007) 635–644, arXiv:hep-ph/0609292 [hep-ph].

[71] B. Allanach, *SOFTSUSY: a program for calculating supersymmetric spectra*, Comput. Phys. Commun. **143** (2002) 305–331, arXiv:hep-ph/0104145 [hep-ph].

[72] M. Muhlleitner, A. Djouadi, and Y. Mambrini, *SDECAY: A Fortran code for the decays of the supersymmetric particles in the MSSM*, Comput. Phys. Commun. **168** (2005) 46–70, arXiv:hep-ph/0311167 [hep-ph].

[73] L. Covi and S. Kraml, *Collider signatures of gravitino dark matter with a sneutrino NLSP*, JHEP **0708** (2007) 015, arXiv:hep-ph/0703130 [HEP-PH].

[74] ATLAS Collaboration, *Search for supersymmetry with jets and missing transverse momentum: Additional model interpretations*, ATLAS-CONF-2011-155. <http://cdsweb.cern.ch/record/1398201>.

[75] H.-C. Cheng, K. T. Matchev, and M. Schmaltz, *Bosonic supersymmetry? Getting fooled at the CERN LHC*, Phys. Rev. **D66** (2002) 056006, arXiv:hep-ph/0205314 [hep-ph].

Appendix A: Control Region $m_{\text{eff}}(\text{incl.})$ plots

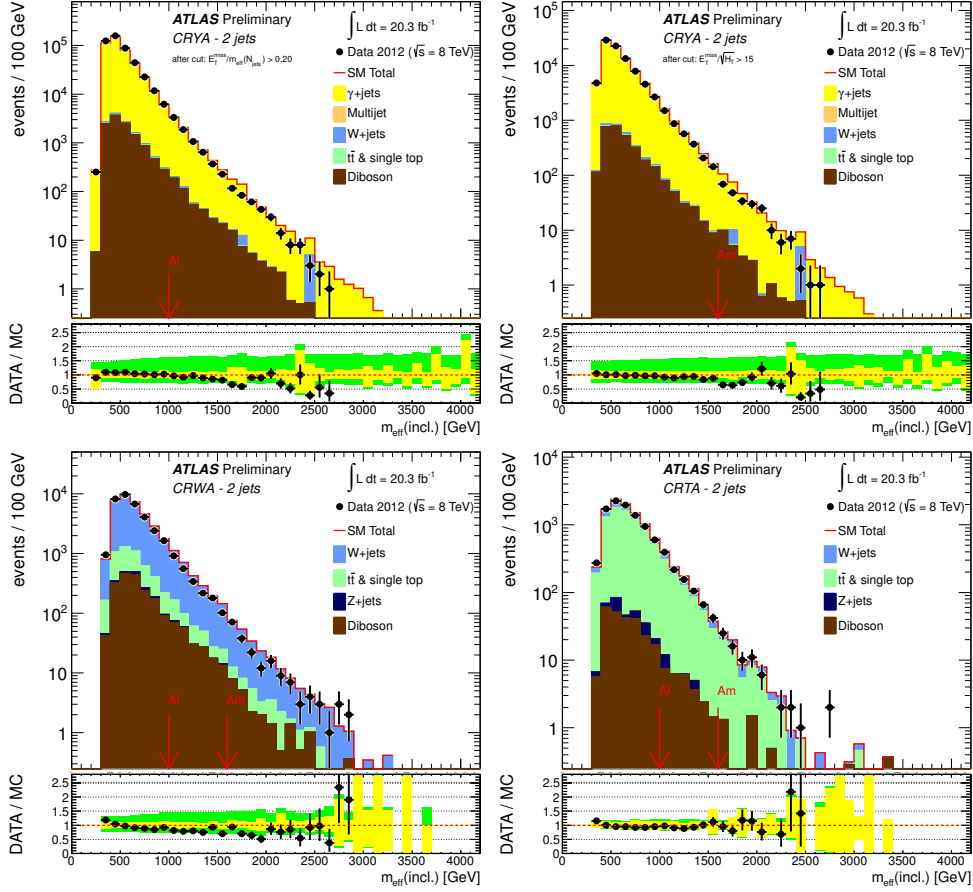


Figure 11: Observed $m_{\text{eff}}(\text{incl.})$ distributions in control regions CRY (top left for ‘loose’ selection criteria, top right for ‘medium’ selection criteria), CRW (bottom left) and CRT (bottom right) corresponding to channel A. The histograms denote the MC background expectations, normalised to cross-section times integrated luminosity. The error bands shown in the lower panels denote the experimental and MC statistical uncertainties in yellow and the total uncertainty including theory uncertainties in green. The red arrows indicate the values at which the requirements on $m_{\text{eff}}(\text{incl.})$ are applied.

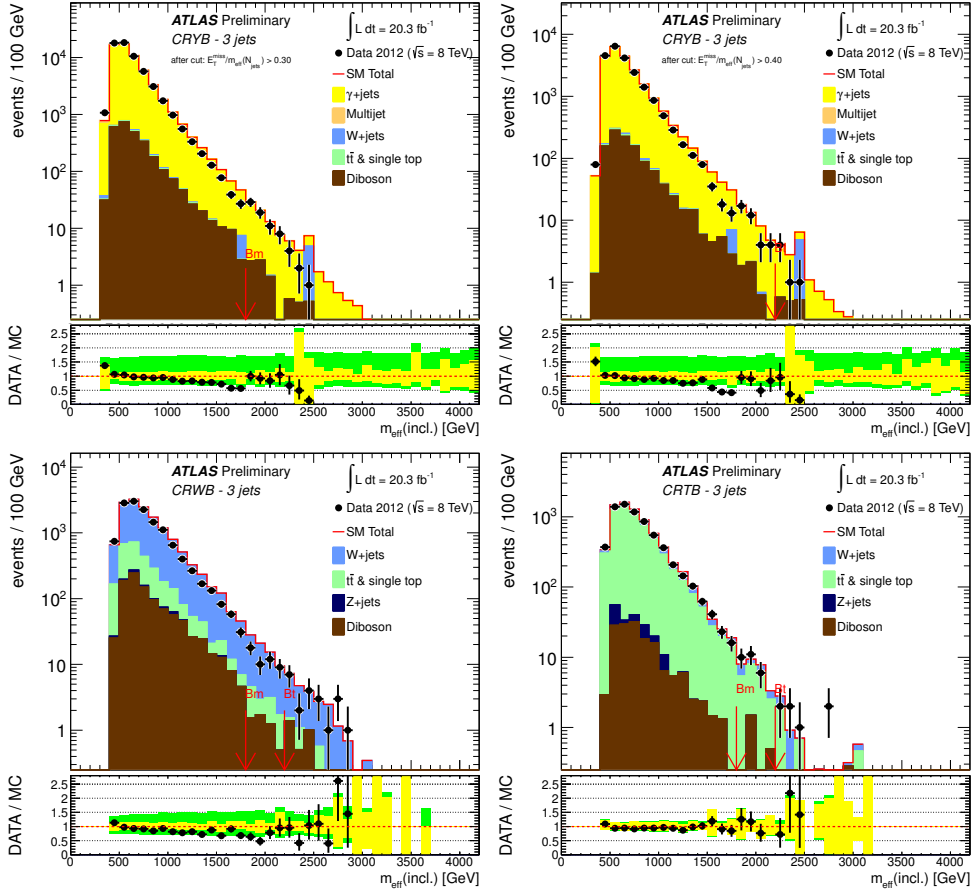


Figure 12: Observed $m_{\text{eff}}(\text{incl.})$ distributions in control regions CRY (top left for ‘medium’ selection criteria, top right for ‘tight’ selection criteria), CRW (bottom left) and CRT (bottom right) corresponding to channel B. The histograms denote the MC background expectations, normalised to cross-section times integrated luminosity. The error bands shown in the lower panels denote the experimental and MC statistical uncertainties in yellow and the total uncertainty including theory uncertainties in green. The red arrows indicate the values at which the requirements on $m_{\text{eff}}(\text{incl.})$ are applied.

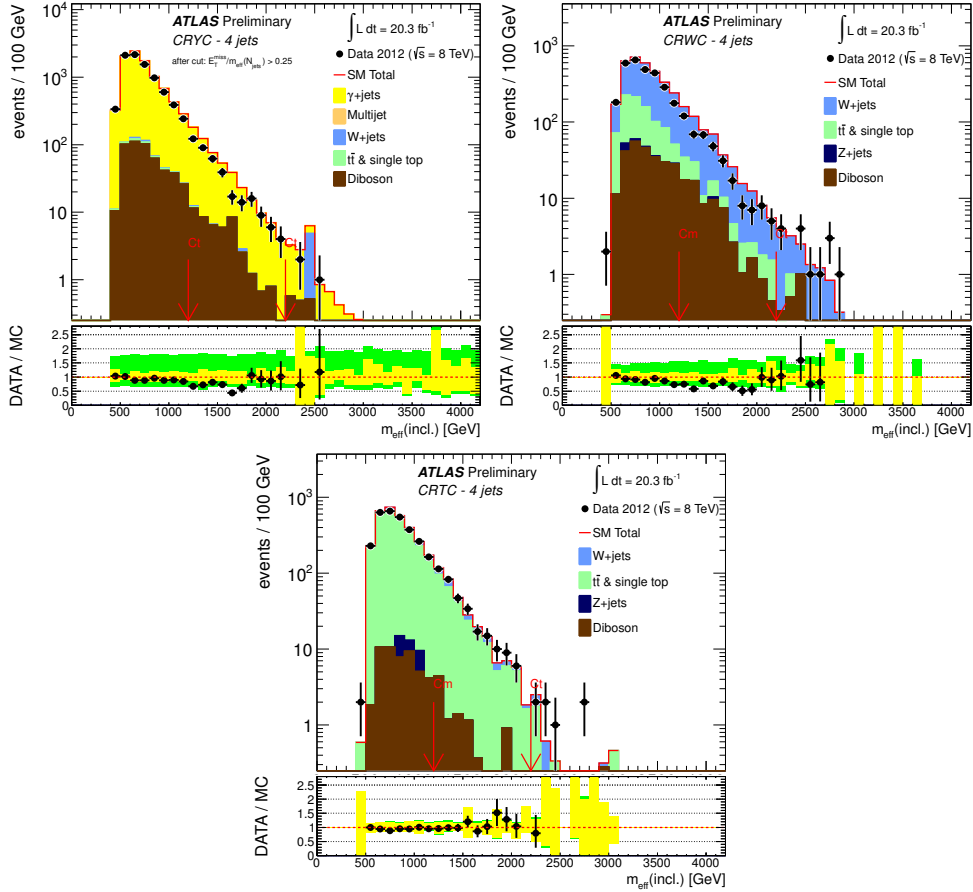


Figure 13: Observed $m_{\text{eff}}(\text{incl.})$ distributions in control regions CRY (top left), CRW (top right) and CRT (bottom) corresponding to channel C. The histograms denote the MC background expectations, normalised to cross-section times integrated luminosity. The error bands shown in the lower panels denote the experimental and MC statistical uncertainties in yellow and the total uncertainty including theory uncertainties in green. The red arrows indicate the values at which the requirements on $m_{\text{eff}}(\text{incl.})$ are applied.

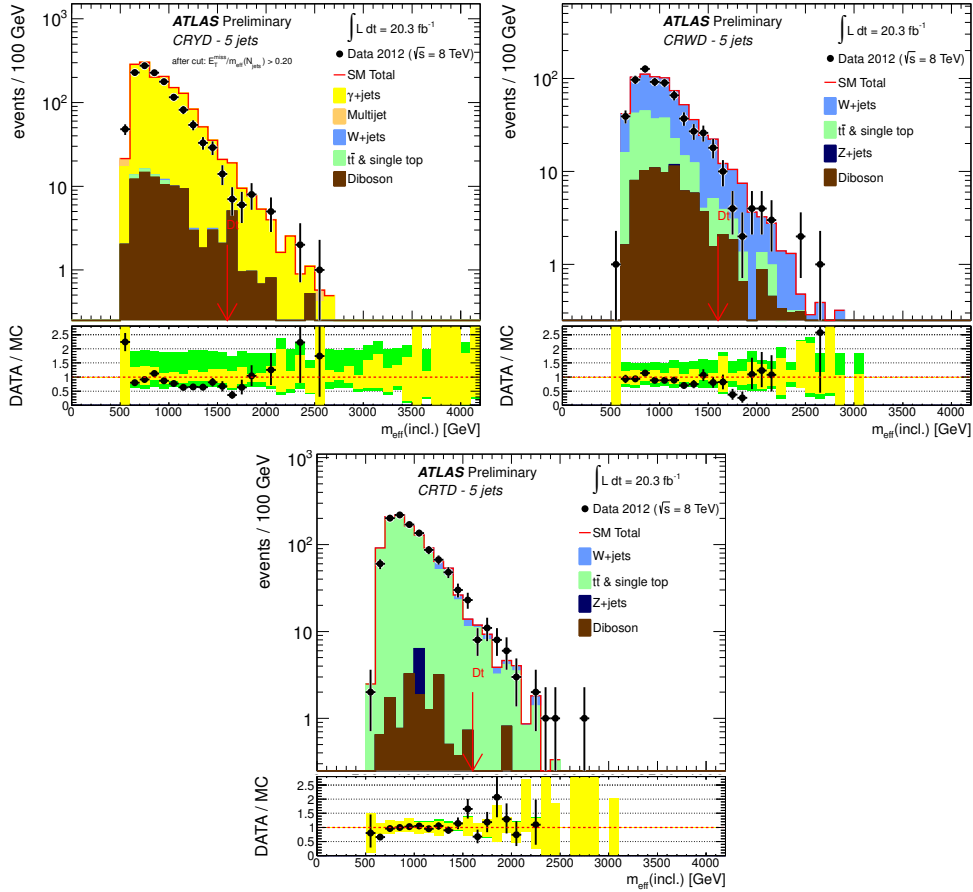


Figure 14: Observed $m_{\text{eff}}(\text{incl.})$ distributions in control regions CRY (top left), CRW (top right) and CRT (bottom) corresponding to channel D. The histograms denote the MC background expectations, normalised to cross-section times integrated luminosity. The error bands shown in the lower panels denote the experimental and MC statistical uncertainties in yellow and the total uncertainty including theory uncertainties in green. The red arrows indicate the values at which the requirements on $m_{\text{eff}}(\text{incl.})$ are applied.

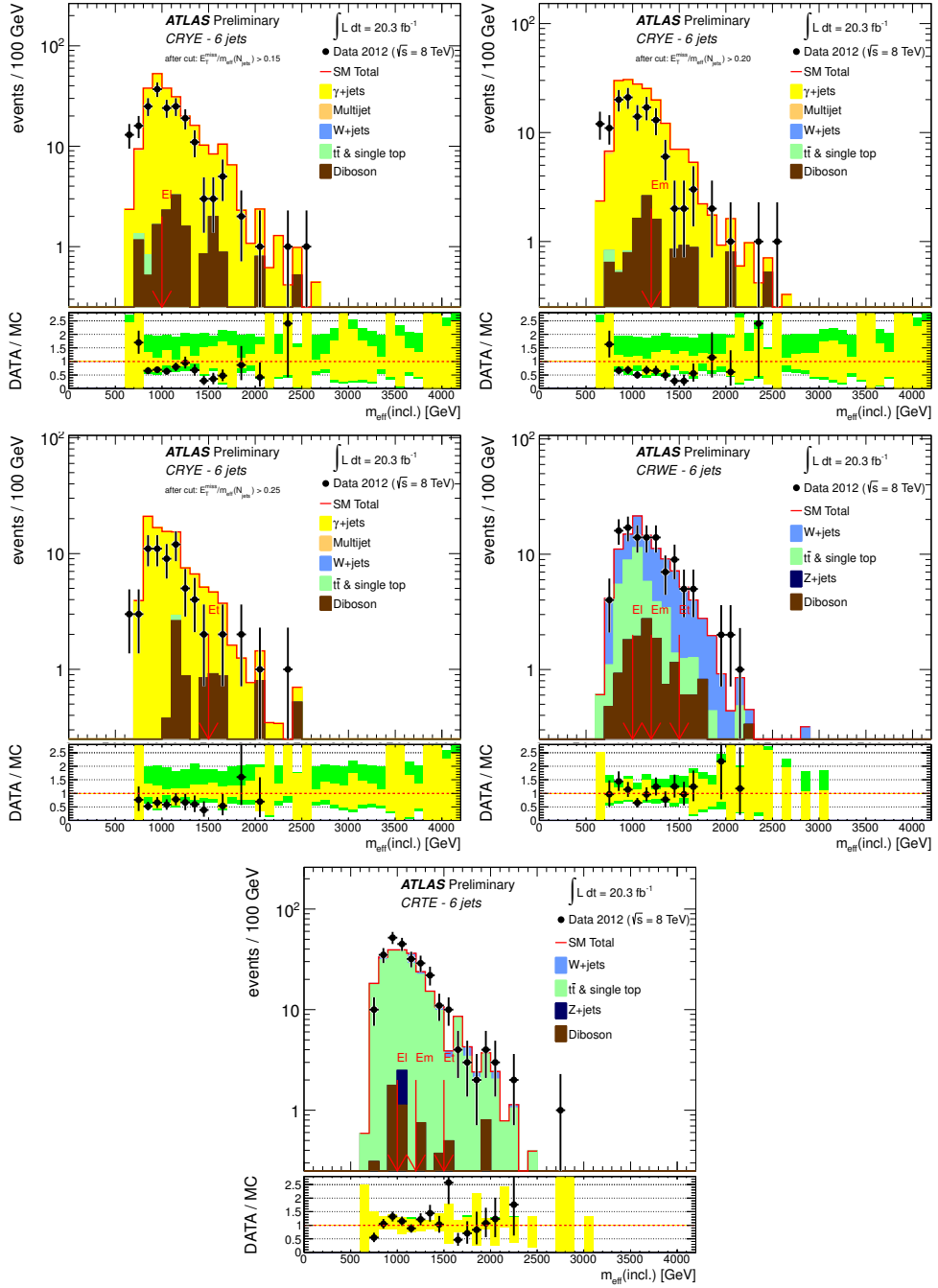


Figure 15: Observed $m_{\text{eff}}(\text{incl.})$ distributions in control regions CRY (top left for ‘loose’, top right for ‘medium’ selection criteria, middle left for ‘tight’ selection criteria), CRW (middle right) and CRT (bottom) corresponding to channel E. The histograms denote the MC background expectations, normalised to cross-section times integrated luminosity. The error bands shown in the lower panels denote the experimental and MC statistical uncertainties in yellow and the total uncertainty including theory uncertainties in green. The red arrows indicate the values at which the requirements on $m_{\text{eff}}(\text{incl.})$ are applied.

Appendix B: Alternative versions of limit plots

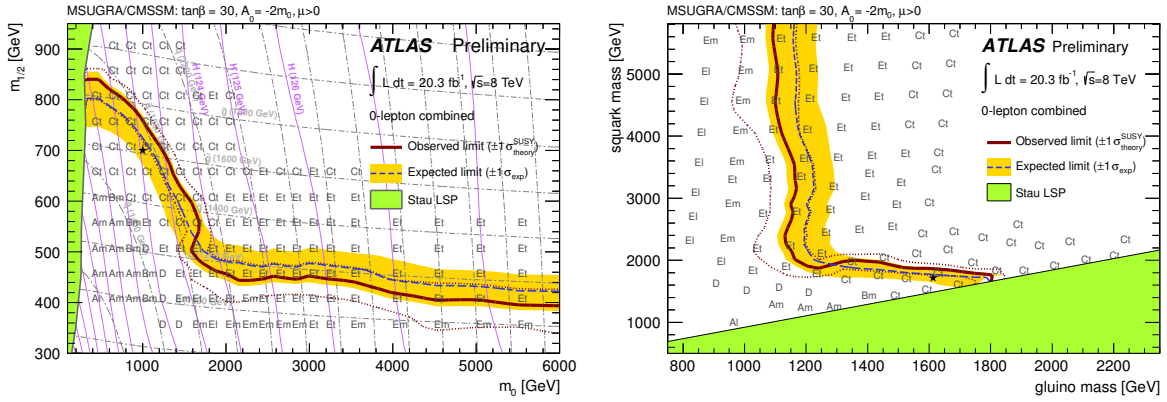


Figure 16: Exclusion limits for MSUGRA/CMSSM models with $\tan\beta = 30$, $A_0 = -2m_0$ and $\mu > 0$ presented (left) in the m_0 – $m_{1/2}$ plane and (right) in the $m_{\tilde{g}}$ – $m_{\tilde{q}}$ plane. Exclusion limits are obtained by using the signal region with the best expected sensitivity at each point. The blue dashed lines show the expected limits at 95% CL, with the light (yellow) bands indicating the 1σ excursions due to experimental and background-theory uncertainties. Observed limits are indicated by medium (maroon) curves, where the solid contour represents the nominal limit, and the dotted lines are obtained by varying the signal cross-section by the theoretical scale and PDF uncertainties. The black star indicates the MSUGRA/CMSSM benchmark model used in Fig. 3(left). The signal regions providing the best expected sensitivity at a selection of model points are indicated.

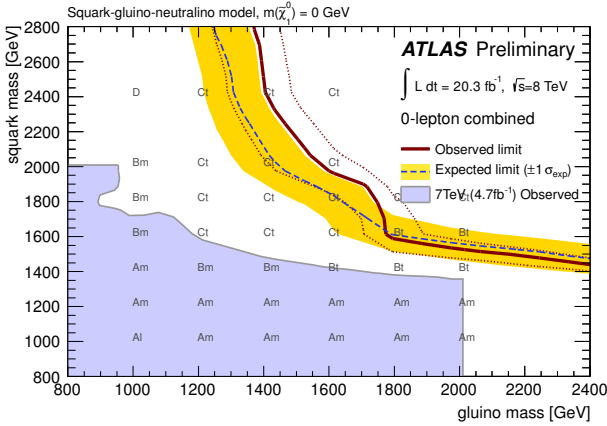


Figure 17: Exclusion limit for a simplified phenomenological MSSM scenario with only strong production of gluinos and first- and second-generation squarks (of common mass), with direct decays to jets and lightest neutralinos. The mass of the lightest neutralino is set to zero. Exclusion limits are obtained by using the signal region with the best expected sensitivity at each point. The dashed line shows the expected limit at 95% CL, with the light (yellow) band indicating the 1σ experimental and background-theory uncertainties. The observed limit is indicated by the solid curve. The dotted lines represent the observed limits obtained by varying the signal cross-section by the theoretical scale and PDF uncertainties. Previous results for $m_{\tilde{\chi}_1^0} = 0$ from ATLAS at 7 TeV [17] are represented by the shaded (light blue) area. Results at 7 TeV are valid for squark or gluino masses below 2000 GeV, the mass range studied for that analysis. The signal regions providing the best expected sensitivity at a selection of model points are indicated.

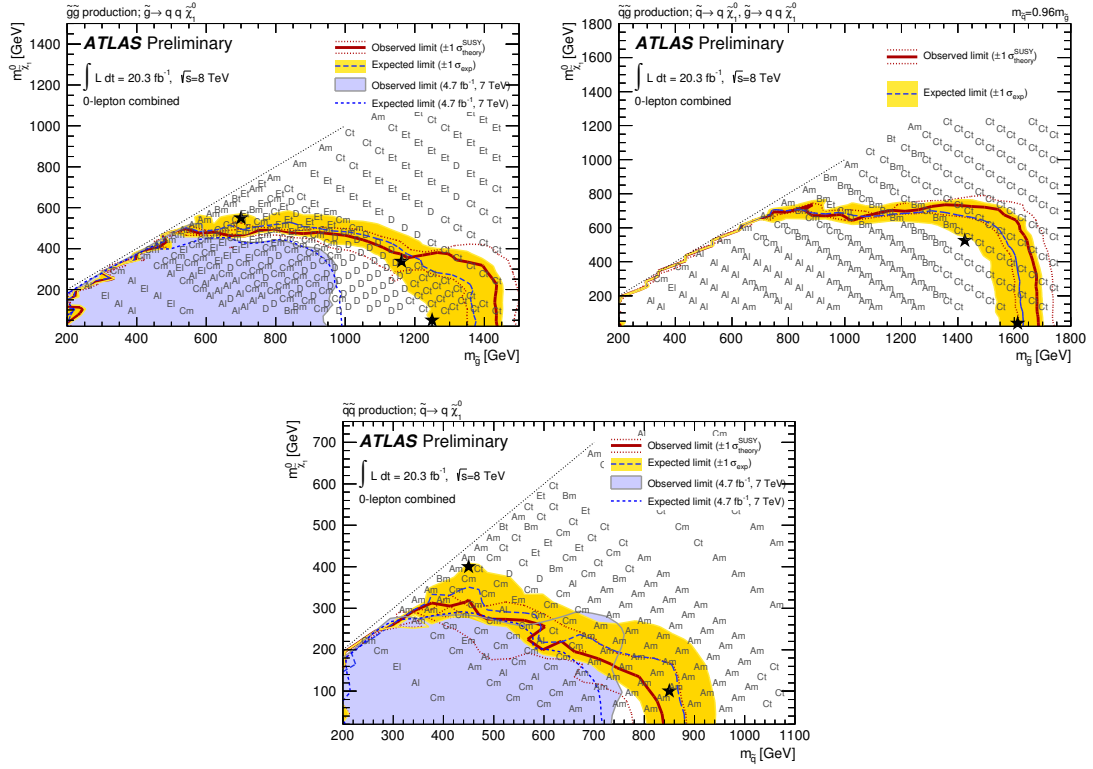


Figure 18: Exclusion limits for direct production of (case a – top left) gluino pairs with decoupled squarks, (case b – top right) light-flavour squarks and gluinos and (case c – bottom) light-flavour squark pairs with decoupled gluinos. Gluinos (light-flavour squarks) are required to decay to two jets (one jet) and a neutralino LSP. Exclusion limits are obtained by using the signal region with the best expected sensitivity at each point. The blue dashed lines show the expected limits at 95% CL, with the light (yellow) bands indicating the 1σ excursions due to experimental and background-theory uncertainties. Observed limits are indicated by medium (maroon) curves, where the solid contour represents the nominal limit, and the dotted lines are obtained by varying the signal cross-section by the theoretical scale and PDF uncertainties. Previous results from ATLAS [17] are represented by the shaded (light blue) areas and light blue dotted lines. The black stars indicate the benchmark models used in Figs. 1–4. The signal regions providing the best expected sensitivity at a selection of model points are indicated.

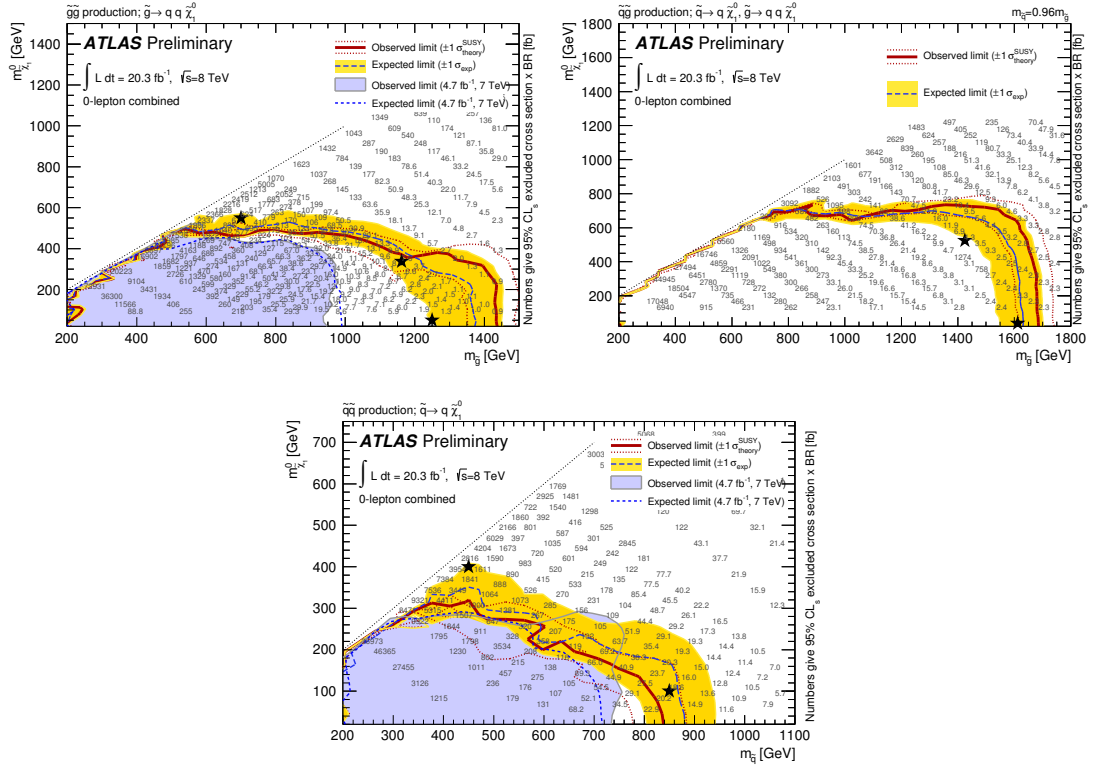


Figure 19: Exclusion limits for direct production of (case a – top left) gluino pairs with decoupled squarks, (case b – top right) light-flavour squarks and gluinos and (case c – bottom) light-flavour squark pairs with decoupled gluinos. Gluinos (light-flavour squarks) are required to decay to two jets (one jet) and a neutralino LSP. Exclusion limits are obtained by using the signal region with the best expected sensitivity at each point. The blue dashed lines show the expected limits at 95% CL, with the light (yellow) bands indicating the 1σ excursions due to experimental and background-theory uncertainties. Observed limits are indicated by medium (maroon) curves, where the solid contour represents the nominal limit, and the dotted lines are obtained by varying the signal cross-section by the theoretical scale and PDF uncertainties. Previous results from ATLAS [17] are represented by the shaded (light blue) areas and light blue dotted lines. The black stars indicate the benchmark models used in Figs. 1–4. The upper limit on the cross-section times branching ratio (in fb) is indicated for each model point.

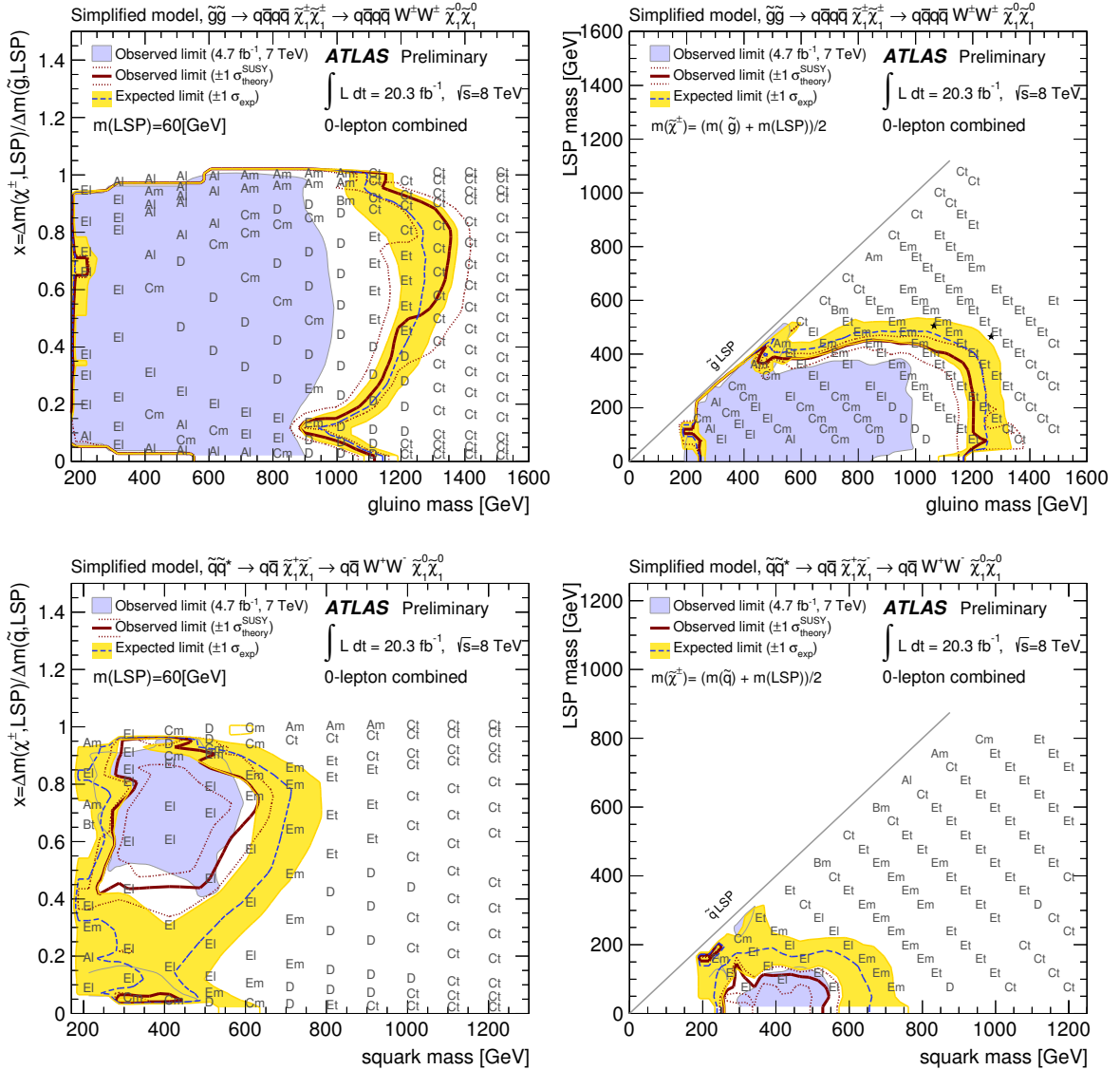


Figure 20: Exclusion limits for pair produced gluinos each decaying via an intermediate $\tilde{\chi}_1^\pm$ to two quarks, a W boson and a $\tilde{\chi}_1^0$ (top) or pair produced light squarks each decaying via an intermediate $\tilde{\chi}_1^\pm$ to a quark, a W boson and a $\tilde{\chi}_1^0$ (bottom). The left-hand figures show results for models with fixed $m(\tilde{\chi}_1^0) = 60$ GeV and varying values of $x = (m_{\tilde{\chi}_1^\pm} - m_{\tilde{\chi}_1^0})/(m_{\tilde{y}} - m_{\tilde{\chi}_1^0})$, where $y = \tilde{g}(y = \tilde{q})$ for the top(bottom) figure. The right-hand plots show results for models with a fixed value of $x = 1/2$ and varying values of $m_{\tilde{\chi}_1^0}$. Exclusion limits are obtained by using the signal region with the best expected sensitivity at each point. The blue dashed lines show the expected limits at 95% CL, with the light (yellow) bands indicating the 1σ excursions due to experimental and background-theory uncertainties. Observed limits are indicated by medium (maroon) curves, where the solid contour represents the nominal limit, and the dotted lines are obtained by varying the signal cross-section by the theoretical scale and PDF uncertainties. Previous results from ATLAS [17] are represented by the shaded (light blue) areas. The signal regions providing the best expected sensitivity at a selection of model points are indicated.

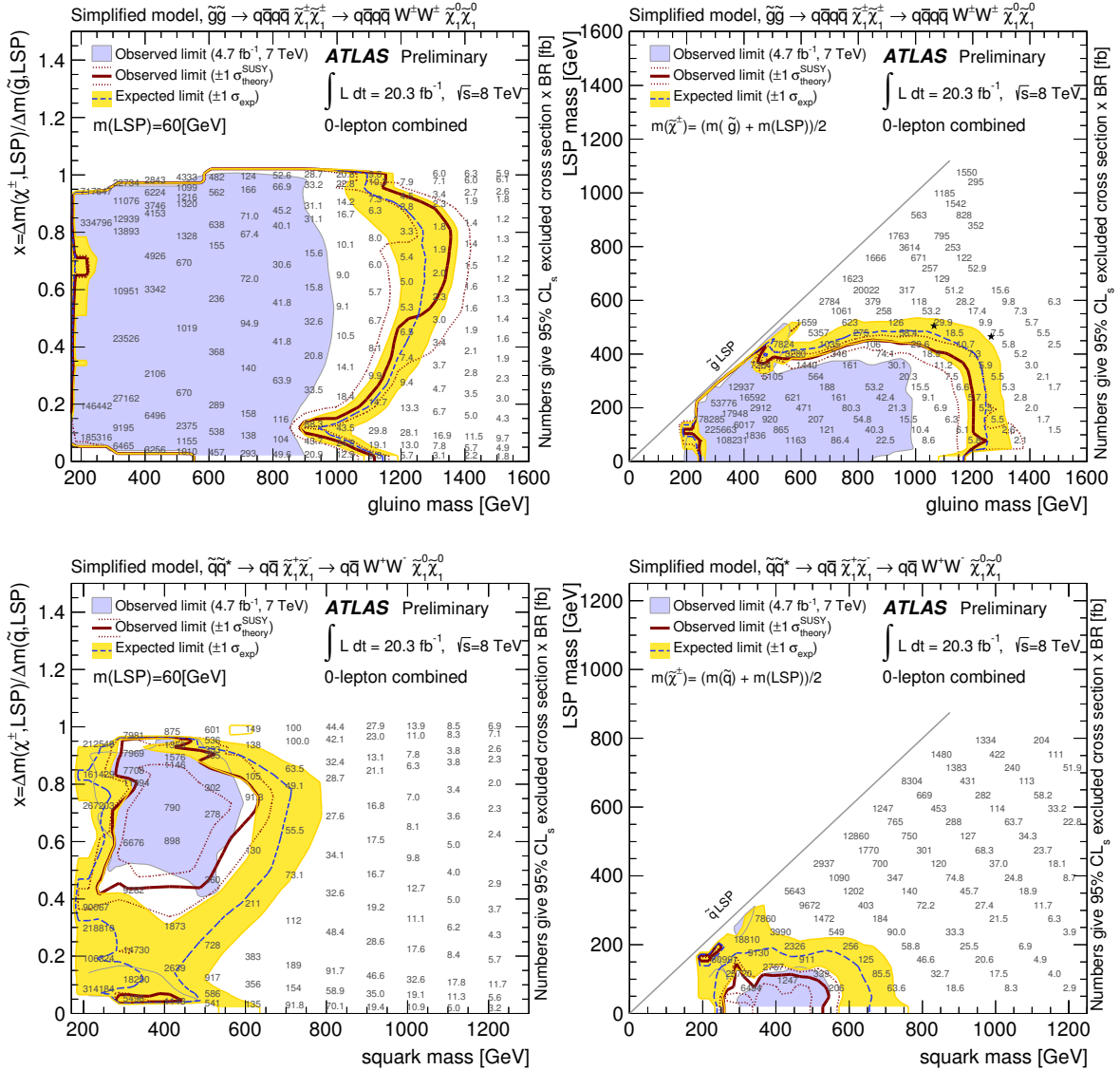


Figure 21: Exclusion limits for pair produced gluinos each decaying via an intermediate $\tilde{\chi}_1^\pm$ to two quarks, a W boson and a $\tilde{\chi}_1^0$ (top) or pair produced light squarks each decaying via an intermediate $\tilde{\chi}_1^\pm$ to a quark, a W boson and a $\tilde{\chi}_1^0$ (bottom). The left-hand figures show results for models with fixed $m(\tilde{\chi}_1^0) = 60$ GeV and varying values of $x = (\tilde{m}_{\tilde{\chi}_1^\pm} - \tilde{m}_{\tilde{\chi}_1^0}) / (m_y - \tilde{m}_{\tilde{\chi}_1^0})$, where $y = \tilde{g}(y = \tilde{q})$ for the top(bottom) figure. The right-hand plots show results for models with a fixed value of $x = 1/2$ and varying values of $m(\tilde{\chi}_1^0)$. Exclusion limits are obtained by using the signal region with the best expected sensitivity at each point. The blue dashed lines show the expected limits at 95% CL, with the light (yellow) bands indicating the 1σ excursions due to experimental and background-theory uncertainties. Observed limits are indicated by medium (maroon) curves, where the solid contour represents the nominal limit, and the dotted lines are obtained by varying the signal cross-section by the theoretical scale and PDF uncertainties. Previous results from ATLAS [17] are represented by the shaded (light blue) areas. The upper limit on the cross-section times branching ratio (in fb) is indicated for each model point.

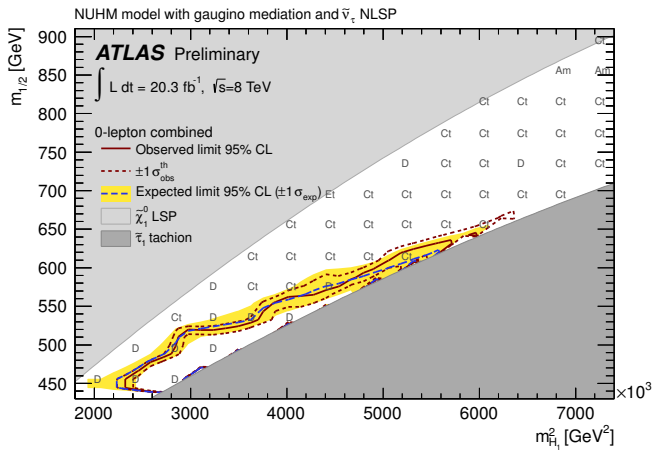


Figure 22: Exclusion limits in the $m_{1/2}$ versus $m_{H_1}^2$ plane for the NUHMG model described in the text. Exclusion limits are obtained by using the signal region with the best expected sensitivity at each point. The blue dashed lines show the expected limits at 95% CL, with the light (yellow) bands indicating the 1σ excursions due to experimental and background-theory uncertainties. Observed limits are indicated by medium (maroon) curves, where the solid contour represents the nominal limit, and the dotted lines are obtained by varying the signal cross-section by the theoretical scale and PDF uncertainties. The signal regions providing the best expected sensitivity at a selection of model points are indicated.

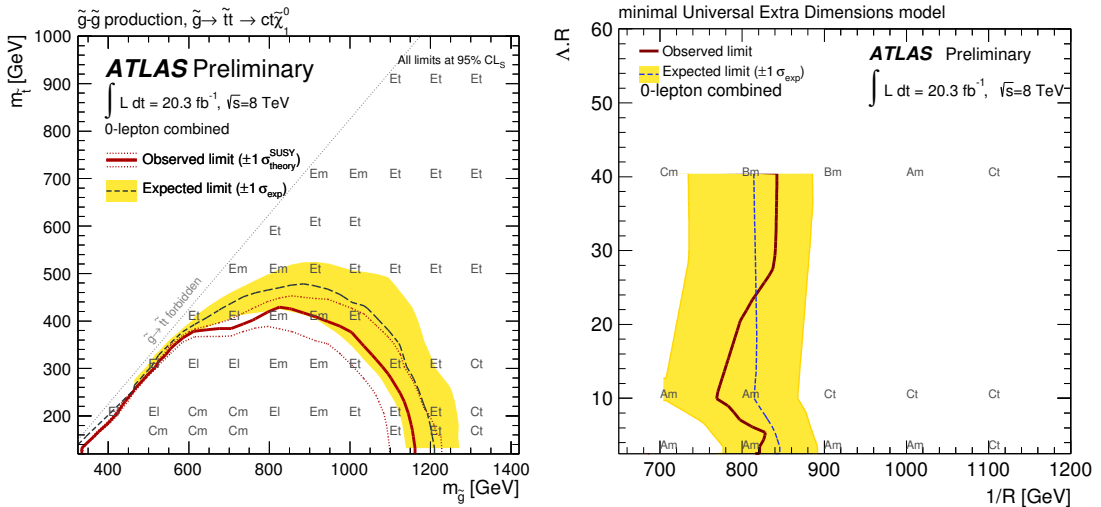


Figure 23: Exclusion limits for pair produced gluinos each decaying into a \tilde{t} and a $\tilde{\chi}_1^0$, with the subsequent decay $\tilde{t} \rightarrow c \tilde{\chi}_1^0$ and $\Delta M(\tilde{t}, \tilde{\chi}_1^0) = 20$ GeV (left), and in the $1/R$ versus $\Lambda \cdot R$ plane for the mUED model described in the text (right). Exclusion limits are obtained by using the signal region with the best expected sensitivity at each point. The blue dashed lines show the expected limits at 95% CL, with the light (yellow) bands indicating the 1σ excursions due to experimental and background-theory uncertainties. Observed limits are indicated by medium (maroon) curves, where the solid contour represents the nominal limit. In the left-hand figure the dotted lines are obtained by varying the signal cross-section by the theoretical scale and PDF uncertainties. In the right-hand figure theoretical uncertainties are not available. Models with $1/R \lesssim 650$ GeV are excluded by previous analyses as described in Ref. [74]. The signal regions providing the best expected sensitivity at a selection of model points are indicated.

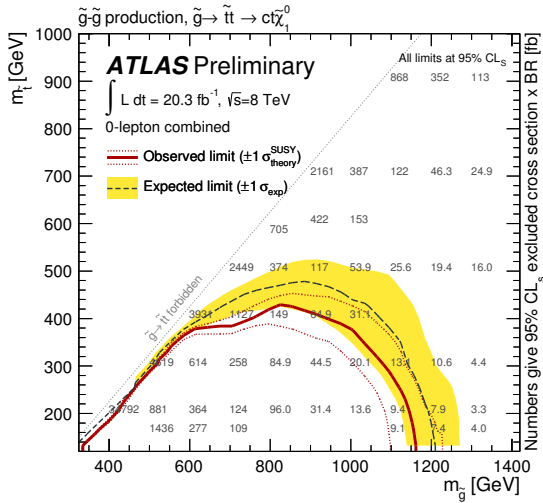


Figure 24: Exclusion limits for pair produced gluinos each decaying into a \tilde{t} and a $\tilde{\chi}_1^0$, with the subsequent decay $\tilde{t} \rightarrow c \tilde{\chi}_1^0$ and $\Delta M(\tilde{t}, \tilde{\chi}_1^0) = 20$ GeV. Exclusion limits are obtained by using the signal region with the best expected sensitivity at each point. The blue dashed lines show the expected limits at 95% CL, with the light (yellow) bands indicating the 1σ excursions due to experimental and background-theory uncertainties. Observed limits are indicated by medium (maroon) curves, where the solid contour represents the nominal limit. The dotted lines are obtained by varying the signal cross-section by the theoretical scale and PDF uncertainties. The upper limit on the cross-section times branching ratio (in fb) is indicated for each model point.

Appendix C: Cut-flow table for selected signal models

Process	$\tilde{q}\tilde{q}$ direct			$\tilde{q}\tilde{q}$ one-step		
Point	$m(\tilde{q})=450 \text{ GeV}$ $m(\tilde{q})=850 \text{ GeV}$ $m(\tilde{q})=662 \text{ GeV}$ $m(\tilde{q})=1612 \text{ GeV}$			$m(\tilde{q})=1425 \text{ GeV}$ $m(\tilde{q})=37 \text{ GeV}$		
	$m(\tilde{\chi}_1^0)=400 \text{ GeV}$ $m(\tilde{\chi}_1^0)=100 \text{ GeV}$ $m(\tilde{\chi}_1^0)=287 \text{ GeV}$ $m(\tilde{\chi}_1^0)=337 \text{ GeV}$			$m(\tilde{\chi}_1^0)=785 \text{ GeV}$ $m(\tilde{\chi}_1^0)=865 \text{ GeV}$ $m(\tilde{\chi}_1^0)=505 \text{ GeV}$ $m(\tilde{\chi}_1^0)=465 \text{ GeV}$		
Number of generated events	20000	5000	10000	5000	5000	20000
Signal Region	A-medium	A-medium	C-medium	B-medium	B-tight	D
In	27288.6 (100.0)	280.4 (100.0)	1944.9 (100.0)	78.0 (100.0)	19.8 (100.0)	122.4 (100.0)
Jet cleaning	27202.0 (99.7)	279.3 (99.6)	1937.1 (99.6)	77.7 (99.7)	19.7 (99.6)	122.1 (99.8)
0 Lepton	24528.0 (89.9)	276.2 (98.5)	1910.0 (98.2)	76.4 (98.0)	19.6 (98.8)	120.5 (98.5)
$E_T^{\text{miss}} > 160 \text{ GeV}$	4082.9 (15.0)	252.0 (89.9)	1569.2 (80.7)	72.7 (93.3)	19.0 (95.9)	108.7 (88.9)
$p_T(j_1) > 130 \text{ GeV}$	3522.7.9 (12.9)	251.6 (89.7)	1555.0 (80.0)	72.7 (93.3)	19.0 (95.8)	108.7 (88.8)
$p_T(j_2) > 60 \text{ GeV}$	2463.8 (9.0)	245.1 (87.4)	1471.1 (75.6)	72.0 (92.4)	18.8 (95.2)	108.6 (88.8)
$p_T(j_3) > 0 - 60 \text{ GeV}$	2463.8 (9.0)	245.1 (87.4)	686.7 (35.3)	53.4 (68.5)	15.0 (75.7)	106.6 (87.1)
$p_T(j_4) > 0 - 60 \text{ GeV}$	2463.8 (9.0)	245.1 (87.4)	223.7 (111.5)	53.4 (68.5)	15.0 (75.7)	90.7 (74.1)
$p_T(j_5) > 0 - 60 \text{ GeV}$	2463.8 (9.0)	245.1 (87.4)	223.7 (111.5)	53.4 (68.5)	15.0 (75.7)	50.1 (40.9)
$p_T(j_6) > 0 - 60 \text{ GeV}$	2463.8 (9.0)	245.1 (87.4)	223.7 (111.5)	53.4 (68.5)	15.0 (75.7)	50.1 (40.9)
$\Delta\phi(j_i, E_T^{\text{miss}}) > 0.4$	1919.9 (7.0)	221.9 (79.2)	196.8 (10.1)	47.0 (60.4)	13.1 (66.2)	41.9 (34.2)
$\Delta\phi(j_i > 40 \text{ GeV}, E_T^{\text{miss}}) > 0 - 0.2$	1919.9 (7.0)	221.9 (79.2)	180.4 (9.3)	47.0 (60.4)	13.1 (66.2)	34.9 (28.6)
$E_T^{\text{miss}} / \sqrt{H_T} > 0 - 15$	723.0 (2.6)	139.8 (49.9)	180.4 (9.3)	47.0 (60.4)	13.1 (66.2)	34.9 (28.6)
$E_T^{\text{miss}} / m_{\text{eff}}(N_j) > 0.15 - 0.4$	723.0 (2.6)	139.8 (49.9)	139.2 (7.2)	34.9 (44.8)	6.3 (31.8)	27.0 (22.1)
$m_{\text{eff}}(\text{incl.}) > 1 - 2.2 \text{ TeV}$	36.2 (0.1)	46.2 (16.5)	57.6 (3.0)	21.4 (27.5)	4.5 (22.8)	16.4 (13.4)
						4.1 (7.9)

Table 5: Cut-flows for expected numbers of events for some model points using the signal region expected to perform best for the model, normalised to $\mathcal{L} = 20.3 \text{ fb}^{-1}$. The absolute efficiency in % is provided in parenthesis.